



# Large scale dynamics of a high Reynolds number axisymmetric separating/reattaching flow

R. Pain, Pierre-Elie Weiss, Sébastien Deck, Jean-Christophe Robinet

## ► To cite this version:

R. Pain, Pierre-Elie Weiss, Sébastien Deck, Jean-Christophe Robinet. Large scale dynamics of a high Reynolds number axisymmetric separating/reattaching flow. *Physics of Fluids*, 2019, 31, pp.125119-1 - 125119-20. 10.1063/1.5121587 . hal-02449003

**HAL Id: hal-02449003**

**<https://hal.science/hal-02449003>**

Submitted on 22 Jan 2020

**HAL** is a multi-disciplinary open access archive for the deposit and dissemination of scientific research documents, whether they are published or not. The documents may come from teaching and research institutions in France or abroad, or from public or private research centers.

L'archive ouverte pluridisciplinaire **HAL**, est destinée au dépôt et à la diffusion de documents scientifiques de niveau recherche, publiés ou non, émanant des établissements d'enseignement et de recherche français ou étrangers, des laboratoires publics ou privés.

## Large scale dynamics of a high Reynolds number axisymmetric separating/reattaching flow

R. Pain,<sup>1</sup> P.-E. Weiss,<sup>1, a)</sup> S. Deck,<sup>1</sup> and J.-C. Robinet<sup>2</sup>

<sup>1)</sup> *ONERA - The French Aerospace Lab - F-92190, Meudon*

<sup>2)</sup> *DynFluid, Arts et Métiers, ParisTech, 75013 Paris, France*

(Dated: 18 November 2019)

A numerical study is conducted to unveil the large scale dynamics of a high Reynolds number axisymmetric separating/reattaching flow at  $M_\infty = 0.7$ . The numerical simulation allows to acquire a high rate sampled unsteady volumetric data set. This huge amount of spatial and temporal information is exploited in the Fourier space to visualize for the first time in physical space and at such a high Reynolds number ( $Re_D = 1.2 \cdot 10^6$ ) the statistical signature of the helical structure related to the anti-symmetric mode ( $m = 1$ ) at  $St_D = 0.18$ . The main hydrodynamic mechanisms are identified through the spatial distribution of the most energetic frequencies, i.e.  $St_D = 0.18$  and  $St_D \geq 3.0$  corresponding to the vortex-shedding and Kelvin-Helmholtz instability phenomena, respectively. In particular, the dynamics related to the dimensionless shedding frequency is shown to become dominant for  $0.35 \leq x/D \leq 0.75$  in the whole radial direction as it passes through the shear layer. The spatial distribution of the coherence function for the most significant modes as well as a three-dimensional Fourier decomposition suggest the global features of the flow mechanisms.

More specifically, the novelty of the study lies in the evidence of the flow dynamics through the use of cross-correlation maps plotted with a frequency selection guided by the characteristic Strouhal number formerly identified in a local manner in the flow field or at the wall. Moreover and for the first time, the understanding of the scales at stake is supported both by a Fourier analysis and a Dynamic Mode Decomposition in the complete three-dimensional space surrounding the afterbody zone.

---

<sup>a)</sup> [peweiss@onera.fr](mailto:peweiss@onera.fr); <http://www.onera.fr/en/staff/pierre-elie-weiss>

## I. INTRODUCTION

The study of axisymmetric afterbody flows is mainly motivated by aerospace problems<sup>1–4</sup>. Indeed, this geometry is a very simplified prototype of the main stage of a space launcher’s after-body. The understanding of the structure of turbulent shear flows with separation and reattachment is of major importance for many engineering applications. In some configurations, the flow is the seat of pressure fluctuations resulting in large non-axisymmetric aerodynamic forces on the structure. The aim of this work is to better understand the physical mechanisms responsible for these pressure fluctuations. Eventually, the knowledge of the spatial organization of the fluctuating flow field permits to guide the design of flow control devices.

Separating/reattaching flows are characterised by the presence of a recirculation region which is governed by a complex dynamics<sup>5,6</sup>. As it is often accompanied by a highly unsteady fluctuating pressure field, it is usually preferable to avoid such unsteadiness as it may induce interfering vibrations on the geometry. Among the wide variety of separation/reattachment scenarios, flow separation induced by a leading edge has been well documented in the last decades. For instance, Armaly *et al.*<sup>7</sup> carried out an experimental investigation of a 3D backward facing step flow and evidenced that the length of the recirculation bubble increases with the Reynolds number in the laminar regime while it decays in the fully turbulent stage. Furthermore, the authors have put forward the limitations of 2D modelling of such flow at  $Re > 400$  for the fact that the recirculation region becomes three-dimensional. By extension to bluff body cases, axisymmetric backward facing step flows are of particular interest since the fluctuations in the recirculation zone interact with the wall of the emerging cylinder and expose the geometry to unsteady loads. Deck and Thorigny<sup>8</sup> showed that there exist some similarities between the subsonic two-dimensional backward facing step flow and its axisymmetric counterpart mainly in terms of the shear layer properties. They also performed a spectral analysis of the fluctuating pressure field for a few sensors located in the vicinity of the recirculation zone. The authors derived some main frequencies whose energetic contribution evolves spatially. In particular, the pressure fluctuations at a normalised frequency based on the largest diameter of the geometry  $St_D = 0.2$  were shown to be associated with the antisymmetric azimuthal mode  $m = 1$ . Later, Weiss *et al.*<sup>9</sup> extended the fluctuating

pressure spectral analysis to the wall which unveiled a highly energetic area for  $St_D = 0.2$  fluctuations related to the *vortex-shedding*. Such area was located approximately in the middle of the recirculation zone ( $0.35 < x/D < 0.75$ ). A linear stability analysis conducted by the authors showed in addition the absolutely unstable nature of the  $m = 1$  azimuthal mode. This result corroborates the investigations on a supersonic axisymmetric wake behind a bluff body by Sandberg and Fasel<sup>10</sup> who suggested the co-existence of both absolutely unstable global modes and convectively unstable shear-layer modes.

From the experimental point of view, Deprés, Reijasse, and Dussauge<sup>11</sup> characterised the axisymmetric backward facing step flow at transonic regime both in terms of statistics (Mean and Root Mean Square wall pressure coefficients) and of spectral content of the wall pressure signal. The flow conditions of this experiment are used in this paper. These authors revealed two main Strouhal numbers. The first one corresponds to the vortex shedding  $St_D \simeq 0.2$ , which they associated with an antisymmetric large scale formation by means of a two-point correlation. The second one is related to the convection of turbulent eddies in the shear layer at  $St_D \simeq 0.6$ . On top of  $St_D \simeq 0.2$ , Deck and Thorigny<sup>8</sup> outlined the contribution of an extra low frequency phenomenon associated with the flapping motion of the mixing layer at  $St_D \simeq 0.07$  observed by Driver, Seegmiller, and Marvin<sup>12</sup> for a planar case. Although the overall unsteady flow phenomena have been addressed in the past, their spatial organisation as well as their time evolution remain not fully understood. Indeed, the identification of characteristic mechanisms of highly turbulent flows is still a great challenge for experimentalists and numericists due to the wide variety of scales to deal with.

The wake developing downstream of a sphere, a disk or more generally a bluff-body develops coherent energetic and compact hairpin type structures. This characteristic is particularly observed when the flow is incompressible or in a low subsonic regime. When the Reynolds number increases but remains at a moderate Mach number (subsonic), the wake initially dominated by hairpin structures type (or double hairpin) disappears gradually giving way to structures like vortex rings. In this regime, the large scales are relatively axisymmetric and intermediate scales developed from shear instabilities and developing non-linearly in the form of vortex structures of the chevron or hairpin type (but much smaller than the previous ones). However, for higher Reynolds numbers  $Re_D \geq 10^4$  several articles

TABLE I. Studies dealing with the helical mode in axisymmetric separating/reattaching flows at several Reynolds numbers. RT : Reattachment Type, Fl: Fluid, So: Solid, E: Experimental, N: Numerical, LS: Linear Stability, D : Disc, ABB : Axisymmetric Bluff Body, ABBWE : Axisymmetric Bluff Body With Extension, TCA: Three-Cylinder Afterbody, S: Sphere, J : Jets, W: Wakes, HMHM: Helical Mode Highlighting Method, 1: Single-point Spectra, 2: Two-point Spectra (i.e. Correlation), 3: Spectral Map, POD or Planar DMD, 4: Volume spectra or Koopman modes (DMD), V: Visualization

Authors	Study	Topology	RT	$Re_D$	$St_D$	HMHM
Achenbach <sup>13</sup>	E	S	Fl	$400 \leq Re_D \leq 5 \times 10^6$	$0.1 \leq St_D \leq 0.2$	1,2,V
Taneda <sup>14</sup>	E	S	Fl	$10^4 \leq Re_D \leq 10^6$	/	V
Fuchs, Mercker, and Michel <sup>15</sup>	E	J + W	Fl	$10^4 \leq Re_D \leq 10^6$	0.3	1,2
Monkewitz <sup>16</sup>	LS	ABB	Fl	$Re_D \leq 3.3 \times 10^3$	$0.17 \leq St_D \leq 0.21$	LS
Berger, Scholz, and Schumm <sup>17</sup>	E	D + S	Fl	$1.5 \times 10^4 \leq Re_D \leq 3 \times 10^5$	0.135	1,2,3,V
Cannon, Champagne, and Glezer <sup>18</sup>	E	D	Fl	$Re_D = 1.32 \times 10^4$	0.15	1,2,V
Weickgenannt and Monkewitz <sup>19</sup>	E	ABB	Fl	$3 \times 10^3 \leq Re_D \leq 5 \times 10^4$	0.25	1,V
Sevilla and Martinez-Bazan <sup>20</sup>	E + LS	ABB	Fl	$500 \leq Re_D \leq 1.2 \times 10^4$	0.25	LS,1,V
Deprés, Reijasse, and Dussauge <sup>11</sup>	E	ABBWE	So	$Re_D = 1.2 \times 10^6$	0.2	1,2
Sandberg and Fasel <sup>10</sup>	N + LS	ABB	Fl	$5000 \leq Re_D \leq 2 \times 10^5$	/	LS,V
Shenoy and Kleinstreuer <sup>21</sup>	N	D	Fl	$10 \leq Re_D \leq 300$	0.113	1,V
Pier <sup>22</sup>	LS	S	Fl	$Re_D \leq 350$	$0.11 \leq St_D \leq 0.21$	LS
Simon <i>et al.</i> <sup>23</sup>	N	ABB	Fl	$Re_D = 2.9 \times 10^6$	0.26	1,2,3
Deck and Thorigny <sup>8</sup>	N	ABBWE	So	$Re_D = 1.2 \times 10^6$	0.2	1,2,3
Weiss <i>et al.</i> <sup>9</sup>	N + LS	ABBWE	So	$Re_D = 1.2 \times 10^6$	0.2	LS,1,2,3
Meliga, Sipp, and Chomaz <sup>24</sup>	N + LS	ABB	Fl	$Re_D = 1.2 \times 10^6$	0.2	LS,1
Meliga, Sipp, and Chomaz <sup>25</sup>	LS	ABB + S	Fl	$Re_D \leq 1500$	$0.063 + 0.11$	LS
Pain, Weiss, and Deck <sup>26</sup>	N	ABBWE	So	$Re_D = 1.2 \times 10^6$	0.2	1,3,4,V
Marié <i>et al.</i> <sup>2</sup>	E	TCA	Fl	$Re_D = 1.2 \times 10^6$	0.2 - 0.5	1,3
Pain, Weiss, and Deck <sup>27</sup>	N	TCA	So	$Re_D = 1.2 \times 10^6$	0.2	1,3,4,V
Statnikov <i>et al.</i> <sup>28</sup>	N	ABBWE	Fl	$Re_D = 1.73 \times 10^6$	$0.25 \leq St_D \leq 0.85$	1,3,V
Present study	N	ABBWE	So	$Re_D = 1.2 \times 10^6$	0.2	1,2,3,4,V

have shown including Yun, Kim, and Choi<sup>29</sup> or Weickgenannt and Monkewitz<sup>19</sup> that the flow develops an anti-symmetric dynamics with an azimuthal wave number  $m = \pm 1$ . The recent work of Statnikov, Meinke, and Schröder<sup>30</sup> does not contradict these conclusions. Then, Seidel *et al.*<sup>31</sup> and Cannon<sup>32</sup> also show the existence of this dynamics of the anti-symmetric (helical) type.

A common feature of axisymmetric wakes with or without an interaction with a solid wall concerns the dominant characteristic large-scale structure identified as a single or double helix corresponding to a shedding-type instability. Such a correspondence results from an

analogy made on the classical frequency range observed in planar base flows. Table I gathers studies investigating the helical mode in axisymmetric separating/reattaching flows. One can note that the vortex spiral has mainly been observed experimentally at low to high Reynolds numbers based on the diameter  $D$  of the axisymmetric body of interest (namely  $O(100) \leq Re_D \leq O(10^6)$ ) on spheres (Taneda<sup>14</sup> and Berger, Scholz, and Schumm<sup>17</sup>), discs (Cannon, Champagne, and Glezer<sup>18</sup> and Berger, Scholz, and Schumm<sup>17</sup>), jets and wakes (Fuchs, Mercker, and Michel<sup>15</sup>), or base flows with a reattachment occurring at a wall (Deprés, Reijasse, and Dussauge<sup>11</sup>, Gentile *et al.*<sup>33</sup>), denoted by ‘solid’, or without (Weickgenannt and Monkewitz<sup>19</sup>, Sevilla and Martinez-Bazan<sup>20</sup>, Grandemange, Gohlke, and Cadot<sup>34</sup>, Grandemange *et al.*<sup>35</sup>, Grandemange, Gohlke, and Cadot<sup>36</sup>, Gentile *et al.*<sup>37</sup>, Gentile *et al.*<sup>38, 39</sup>, Rigas *et al.*<sup>40</sup>, Rigas, Morgans, and Morrison<sup>41</sup>), denoted by ‘fluid’. In the aforementioned studies a predominant dimensionless Strouhal number based on  $D$  has been returned through single-point spectral analyses in the range  $[0.1, 0.25]$ . Such a frequency range was confirmed analytically thanks to linear stability studies as in Monkewitz<sup>16</sup> and Sandberg and Fasel<sup>10</sup> on subsonic and supersonic base flows, respectively, Meliga, Sipp, and Chomaz<sup>25</sup> on axisymmetric wakes, Pier<sup>22</sup> on a sphere and Weiss *et al.*<sup>9</sup> on an axisymmetric backward facing step. The characteristic properties of the helix for  $Re_D \leq 10^4$  can be clearly distinguished due to the fact that the spectral content intrinsic to the flow is not as broad as for high Reynolds number flows, i.e.  $Re_D \geq 10^6$ . Indeed, a direct observation or a phase-locked visualization performed on the streamwise velocity (Weickgenannt and Monkewitz<sup>19</sup>) allows to evidence the helical mode.

However, at higher Reynolds numbers, a deep signal analysis becomes mandatory due to the wide variety of scales involved. Hence, for afterbody flows at  $Re_D = O(10^6)$ , Simon *et al.*<sup>23</sup>, Deck and Thorigny<sup>8</sup>, Weiss and Deck<sup>42</sup> and Weiss *et al.*<sup>9</sup> have realised various spectral analyses based on numerical studies using Zonal Detached Eddy Simulation (ZDES) (Deck<sup>43</sup>, Deck<sup>44</sup>). Single-point spectra have permitted to reveal the predominant frequencies in the flow ( $St_D = 0.08, 0.2, 0.6$  corresponding to the flapping, shedding, and breathing of the recirculation bubble which is enclosed by an impinging shear layer, respectively). Two-point correlations evidenced the modal organisation of the flow in the azimuthal direction. Spectral maps allowed to access to the signature of the fluctuating pressure at the wall. This has permitted to identify a potential area of receptiveness of the separated flow

related to an absolute instability. Similar results regarding the frequencies leading the flow dynamics are reported by Marié *et al.*<sup>2</sup> with a POD analysis applied to the flow surrounding a simplified generic launcher configuration. Finally, Pain, Weiss, and Deck<sup>26</sup> presented a methodology based on either 3D Fourier analysis or Dynamic Mode Decomposition (DMD) to identify the occurrence of helical features in broadband spectrum flows which has allowed to map the most excited frequency in the separated area of a three-cylinder afterbody (see Pain, Weiss, and Deck<sup>27</sup>) and, even more recently, a supersonic base flow (see Statnikov *et al.*<sup>28</sup>) or a generic transonic backward-facing step configuration (see Statnikov *et al.*<sup>45</sup>).

Thus, the evidence as well as the space-time organisation of a helical mode at high Reynolds number on an axisymmetric base flow with a solid reattachment has only been conjectured through local analyses of the spectral content.

In this context, the hereby study aims at drawing a detailed profile of the whole three-dimensional unsteady pressure field in axisymmetric backward facing step flows in order to uncover the helix properties at high Reynolds number.

First, a simulation overview is provided in § II with a description of the test case and salient features of the flow. Then, § III is dedicated to the analysis of the spatial organisation of the fluctuating flow. The energy distribution in the Fourier space and the three-dimensional azimuthal coherence organisation are thoroughly analysed in the neighbourhood of the axisymmetric step. The last part of this paper (§ IV) is devoted to the modal decomposition of the whole pressure field. Finally, results are summarized in § V together with a discussion about the leading flow mechanisms.

## II. SIMULATION OVERVIEW

### A. Test case and description of the computation

The geometry studied consists of an axisymmetric backward facing step similar to the existing experimental S3Ch wind tunnel configuration studied by Deprés, Reijasse, and Dussauge<sup>11</sup> and Meliga and Reijasse<sup>46</sup>. This configuration is composed of a cylinder extended

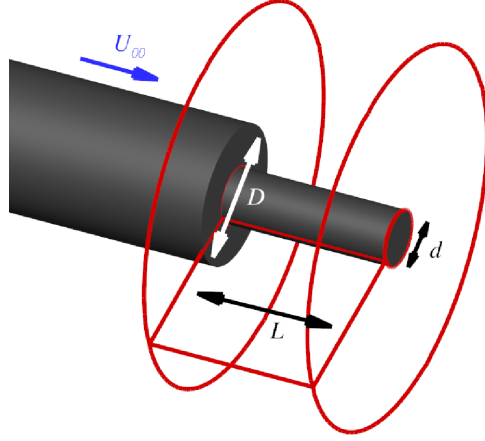


FIG. 1. Geometry of the axisymmetric backward facing step with a downstream cylinder of finite length.  $L/D = 1.2$  and  $\frac{d}{D} = 0.4$  ; ( $\rightarrow$ ) main direction of the flow with  $U_\infty$  corresponding to the free stream velocity. The red edges define the bounds of the domain where the instantaneous flow data was sampled.

by another cylinder of finite length and smaller diameter as represented in figure 1. The characteristic aspect ratios are  $\frac{L}{D} = 1.2$  and  $\frac{d}{D} = 0.4$ ,  $L$  being the length of the smallest cylinder,  $D$  and  $d$  the diameters of the largest and smallest cylinder, respectively. The hereby study focuses on the transonic flow regime with a free stream Mach number  $M_\infty$  equal to 0.7. The Reynolds number based on  $D$  is  $Re_D = 1.2 \cdot 10^6$  and the boundary layer thickness at the edge of the largest cylinder is  $\frac{\delta_0}{D} = 0.2$ . The free-stream dynamic pressure is  $q_\infty = \frac{\gamma}{2} M_\infty^2 P_\infty \approx 24,815$  Pa.

The size of the computational domain represented in figure 2 together with a close-up of the mesh in the afterbody zone is approximately equal to  $29D$  in the streamwise direction and  $10D$  in the radial direction. The backward facing step beginning at the end of the larger cylinder is located at  $x = 174.3D$  with respect to the inflow which permits to obtain the expected values of the integral properties of the boundary layer at the separation point.

The numerical simulation contains four types of boundary conditions:

1. At the inlet : a condition based on an uniform thermodynamic state defined using stagnation quantities
2. At the wall : a no-slip adiabatic condition



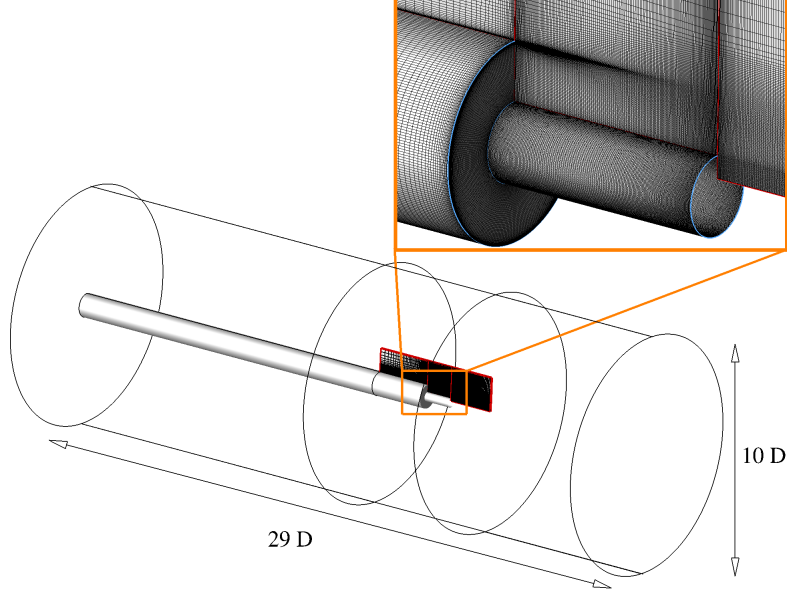


FIG. 2. Sizes of the computational domain and close-up view of the mesh in the separated zone of interest

3. On top of the domain in the normal direction : a non-reflecting boundary condition to avoid spurious wave reflections
4. At the outlet : a far field condition

The present analysis is focused on the deep understanding of the flow dynamics in the separated area located in the neighbourhood of the smallest cylinder (see figure 1). This volume of interest contains  $N_i \times N_j \times N_k = 171 \times 112 \times 240$  points with a streamwise length  $L_x = 1.2D$ , a radial extent  $L_r = 1.05D$  and  $l_\theta = 0.4\pi D$  and  $L_\theta = 2.5\pi D$  for the inner and outer perimeters, respectively. The entire computational domain for this study is made up of a multi-block structured grid containing  $12 \cdot 10^6$  cells. For the ZDES approach of such a configuration a grid sensitivity study has already been performed by Deck and Thorigny<sup>8</sup>. These authors used three grids containing 5.5, 7 and 8.3 million points showing a convergence for the first- and second-order statistics of the pressure (i.e.  $C_p$  and  $C_{p_{rms}}$ ). The present grid has been generated taking into account this previous result. The azimuthal direction, which has formerly been identified as a crucial one beside the streamwise direction for the flow dynamics (Fuchs, Mercker, and Michel<sup>15</sup>, Berger, Scholz, and Schumm<sup>17</sup>), is discretised with 240 points providing a resolution of  $1.5^\circ \text{ cell}^{-1}$ . Moreover, the separated areas have

been designed to follow the LES requirements in terms of number of points and cell isotropy. As advised by Simon *et al.*<sup>23</sup>, the early stages of the vorticity thickness development are modelled with 15 points.

As represented in figure 3, this resolution rapidly increases with the mixing layer growth reaching almost 60 points in the radial direction after the middle of the extension ( $x/D \approx 0.6$ ). In practice, the grid resolution is not calculated adaptively. The vorticity thickness  $\delta_\omega = \Delta U / \max_y(\frac{\partial U}{\partial y})$  is plotted with  $\Delta U = U_1 - U_2$  where  $U_1$  and  $U_2$  stand for the characteristic streamwise velocities on both sides of the shear layer.  $U_1$  is approximately equal to  $237 \text{ m.s}^{-1}$  and  $U_2$  varies rapidly from  $-78 \text{ m.s}^{-1}$  to  $5 \text{ m.s}^{-1}$ . Then, selected resolution is related to the aforementioned empirical observation performed by Simon *et al.*<sup>23</sup>. The number of points clustered in the mixing layer grows rapidly due to the topology which has been adapted to encompass the shear layer. The time-averaged location of the shear has been determined on the basis of a preliminary RANS simulation with the same mesh. Such a grid refinement has been shown by Lele<sup>47</sup> to be sufficient to discretise the layer of fluid linking the vortices inside the mixing layer (i.e. the braids). Indeed, the author used 7 to 8 grid points to resolve the braid region whereas in the present case, the radial discretisation rapidly exceeds 20 points after the separation occurring at the end of the larger cylinder. Finally, the grid parameters in wall units for  $x \leq 0$  in the region treated using ZDES mode 0 (i.e. URANS) are  $(\Delta x^+, \Delta r^+, \Delta s^+) = (130, 4, 200)$ . The minimum and the maximum values of  $\Delta x/D$ ,  $\Delta r/D$  and  $\Delta s/D$  (where  $s = \theta D/2$  stands for the grid arc distance) are  $(\Delta x/D, \Delta r/D, \Delta s/D)_{\min} = (0.003, 0.00015, 0.01309)$  and  $(\Delta x/D, \Delta r/D, \Delta s/D)_{\max} = (0.2, 0.5, 0.1309)$ . It has to be noted that the dominant azimuthal wavelength along the streamwise direction found in the following is  $\lambda_\theta = \pi D/2$ . As a consequence, the dimensionless wavelength of interest is  $\lambda_\theta/D \approx 1.57$  which has to be compared to the azimuthal resolution characterised by the grid arc distance which is approximately 100 times lower (i.e.  $\Delta s/D \approx 0.013$ ) in the mixing layer region. Such a resolution allows to simulate the upstream attached boundary layer in RANS mode. The separation is sharp on such a configuration which means that the integral properties of the upstream boundary layer are the most important to reproduce the flow features. The boundary layer thickness at the separation ( $\delta/D = 0.2$ ) is the one predicted by the RANS calculation based on the Spalart-Allmaras turbulence which is well acknowledged to predict attached flows. Given the location of the separation is prescribed by the geometry, the integral properties of the

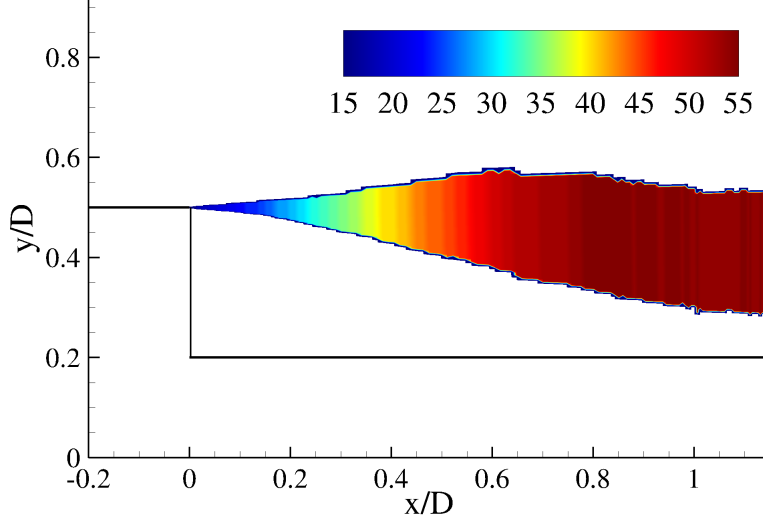


FIG. 3. Streamwise evolution of the number of points clustered in the vorticity thickness  $\delta_\omega = \Delta U / \max_y(\frac{\partial U}{\partial y})$  with  $\Delta U = U_1 - U_2$  where  $U_1$  and  $U_2$  stand for the characteristic streamwise velocities on both sides of the shear layer.

upstream boundary layer is of first importance compared to fluctuations. Such a point has been investigated experimentally by Morris and Foss<sup>48</sup>. These authors have shown that the interaction between a separated turbulent flow and the fluctuations in an upstream boundary layer can be assumed to be negligible for high Reynolds number flows. This supports the fact that no additional synthetic fluctuations are needed in the incoming boundary layer. In practice, Holmes, Lumley, and Berkooz<sup>49</sup> suggested the existence of a communication between a mixing layer and a boundary layer for a laminar separation and argued that this is not true for high Reynolds number turbulent boundary layers. As a consequence, a slow depletion of  $C_p$  is indeed observed which evidences the strong influence of the recirculation zone on the incoming boundary layer which concerns the properties of the mean part of the flow field and not the fluctuating one. Finally, Scharnowski *et al.*<sup>50</sup> performed a numerical simulation on a similar test case with a longer extension for the same Mach number namely  $M_\infty = 0.7$  using Synthetic Turbulence Generation and obtained no difference in the recompression process (i.e. the same slow depletion of  $C_p$  with the same levels).

## B. General description of the numerical set up

The finite-volume solver FLU3M code developed by ONERA<sup>51</sup> is used to solve the compressible Navier-Stokes equations on multi-block structured grids. Time integration is performed by means of a second-order accurate backward Gear scheme. Spatial discretisation is obtained by a modified AUSM+ scheme proposed by Liou<sup>52</sup>. The accuracy of the solver for multi-resolution calculations has been assessed in various applications including afterbody flows<sup>8,23,53</sup>. In these last references, the numerical results are thoroughly compared to the available experimental data including spectral and second-order analysis.

The approach used to model this flow is the Zonal Detached Eddy Simulation (ZDES) proposed by Deck<sup>43,44</sup> which belongs to the RANS/LES approaches (see Sagaut, Deck, and Terracol<sup>54</sup> for a review). Within ZDES three different length scale formulations entering the destruction term of the eddy viscosity equation, also called modes, are optimised to be employed on three different flow topologies (Deck<sup>44</sup>, Deck *et al.*<sup>55</sup>).

The selection process of the chosen mode is guided by the intrinsic nature of the flow separation (see figure 4). The separation locus can be either triggered by the geometry (ZDES mode I), a pressure gradient on a smooth surface (ZDES mode II) or the dynamics of an incoming boundary layer (ZDES mode III). This latter mode can be interpreted as a Wall-Modelled Large Eddy Simulation (WMLES) (Deck *et al.*<sup>56</sup>, Deck *et al.*<sup>57</sup>).

An example, where all these modes are used in the same calculation, is provided in Deck and Laraufie<sup>58</sup> in the frame of a three-element airfoil.

As a consequence, the present case is treated using ZDES mode I (for  $x > 0$ ) meaning the area located downstream the separation point is computed with LES while the area upstream (for  $x < 0$ ) is solved using the URANS approach (mode 0 of ZDES).

## C. Salient features of the flow

As a first glimpse to the global dynamics of the axisymmetric separating / reattaching flow, an overview of the flow topology is provided in figure 5 (*a*) with the visualisation of an iso-surface of the normalised  $Q$ -criterion ( $QU_\infty^2/D^2 = 50$ ) coloured by the streamwise velocity component coupled with a numerical pseudo-schlieren in a streamwise cut-off plane

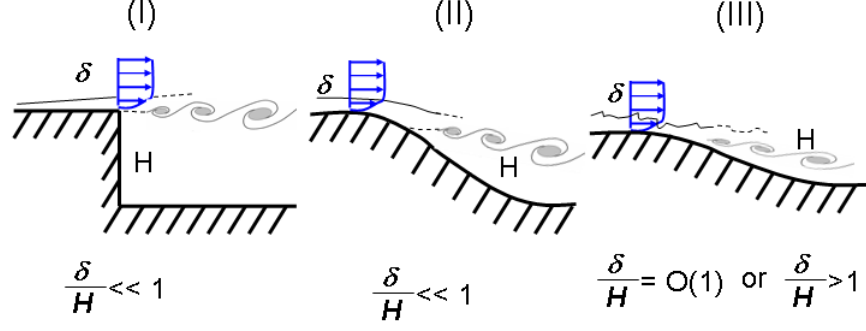


FIG. 4. Taxonomy of classical separated flows. I: separation fixed by the geometry, II: separation induced by a pressure gradient on a curved surface, III: separation strongly influenced by the dynamics of the incoming boundary layer (adapted from Deck<sup>44</sup>).

and at the wall. The dimensionless  $Q$ -criterion is represented in order to evidence the coherent structures of the instantaneous flow.  $Q$  is a second-order invariant of the velocity gradient tensor  $\nabla \mathbf{u}$  and is defined as follows:

$$Q = \frac{1}{2}(\Omega_{ij}\Omega_{ij} - S_{ij}S_{ij}) = -\frac{1}{2}\frac{\partial u_i}{\partial x_j}\frac{\partial u_j}{\partial x_i} > 0 \quad (1)$$

where  $S_{ij}$  and  $\Omega_{ij}$  are respectively the symmetric and antisymmetric components of  $\nabla \mathbf{u}$ .

It is observed that the coherent structures originating from the edge of the body feature a toroidal shape and rapidly distort to become fully three-dimensional as they are convected downstream. The numerical pseudo-schlieren allows to visualise the wide diversity of length scales in the flow and enables to picture the unsteadiness of the position of the solid reattachment point. Figure 5 (b) provides the mean and instantaneous organisation of the flow in a cut-off plane. First, the visualisation of the isolines of  $QU_\infty^2/D^2$  is coupled with the representation of four main locations where unsteady phenomena (*Kelvin-Helmholtz* instability, shear layer *flapping* motion, *impact* of coherent structures on the wall, and *vortex-shedding*) are dominating. The mean streamlines evidence the different recirculation regions that are located around the geometry. Finally, figure 5 (c) presents the streamwise evolution of the mean  $Cp = \frac{p-p_\infty}{q_\infty}$  and fluctuating  $Cp_{RMS} = \frac{p_{RMS}}{q_\infty}$  wall pressure coefficients. Three characteristic areas can be distinguished. For  $x/D \leq 0$ , a slow depletion of  $Cp$  is observed which evidences the strong influence of the recirculation zone on the integral properties of the incoming boundary layer. After the separation,  $Cp$  values decrease due to the acceleration of the backflow for  $x/D \in [0, 0.55]$ . Then, a recompression process dominates the mean pres-

sure field at the wall until  $x/D \approx 1, 2$ . Concerning the root mean square coefficient of the fluctuating pressure  $Cp_{RMS}$ , a steady increase is observed in the range  $x/D \in [0, 0.85]$  due to the organised shear layer structures (Hudy, Naguib, and Humphreys<sup>59</sup>). This monotonic growth ends with the occurrence of a plateau in the area  $x/D \in [0.85, 1.1]$ . Such a behaviour is observed for many separated flows (Mabey<sup>60</sup>, Coe<sup>61</sup> among others). For both quantities, i.e. mean and rms pressure, ZDES reproduces well the experimental distribution shown in Deprés, Reijasse, and Dussauge<sup>11</sup> and Meliga and Reijasse<sup>46</sup>.

One can observe from figure 5 (b) that the present geometry and flow regime involve a solid mean reattachment point which is located at approximately  $x/D = 1.1$ .

The literature related to axisymmetric backward facing step flows provides a background knowledge for the hereby dynamics analysis. Four normalised frequencies based on the greatest diameter  $D$  were identified to be responsible for the most energetic loads applied on the afterbody. The areas where each frequency is dominant were located and associated with coherent structure scales. For instance Deprés, Reijasse, and Dussauge<sup>11</sup> related the large scale vortices in the wake region to  $St_D = 0.2$ . Weiss *et al.*<sup>9</sup> evidenced the absolute nature of the  $m = 1$  antisymmetric mode mainly responsible for the side loads and associated with  $St_D = 0.2$  by means of a local linear stability analysis. Furthermore, these latter authors confirmed the helical behaviour of the absolute instability as suggested by previous studies<sup>14,17</sup>.

Huerre and Rossi<sup>63</sup> carried out a stability analysis on a free shear layer and derived an expression for the evolution of the frequency  $f$  in the streamwise direction as a function of the vorticity thickness of the shear layer (denoted  $\delta_\omega$ ).

These authors thus put forward that the Kelvin-Helmholtz instability which occurs in the mixing layer originating from the separation point at the edge of the cylinder of diameter  $D$  is characterised by the range of normalised frequency  $6 < St_D < 8$ .

The frequency range around  $St_D = 0.07$  was linked to the mixing layer flapping motion as exposed by Driver, Seegmiller, and Marvin<sup>12</sup>. Finally, it was evidenced by Deck and Thorigny<sup>8</sup> that the reattaching point on the emerging cylinder oscillates at  $St_D = 0.6$ .

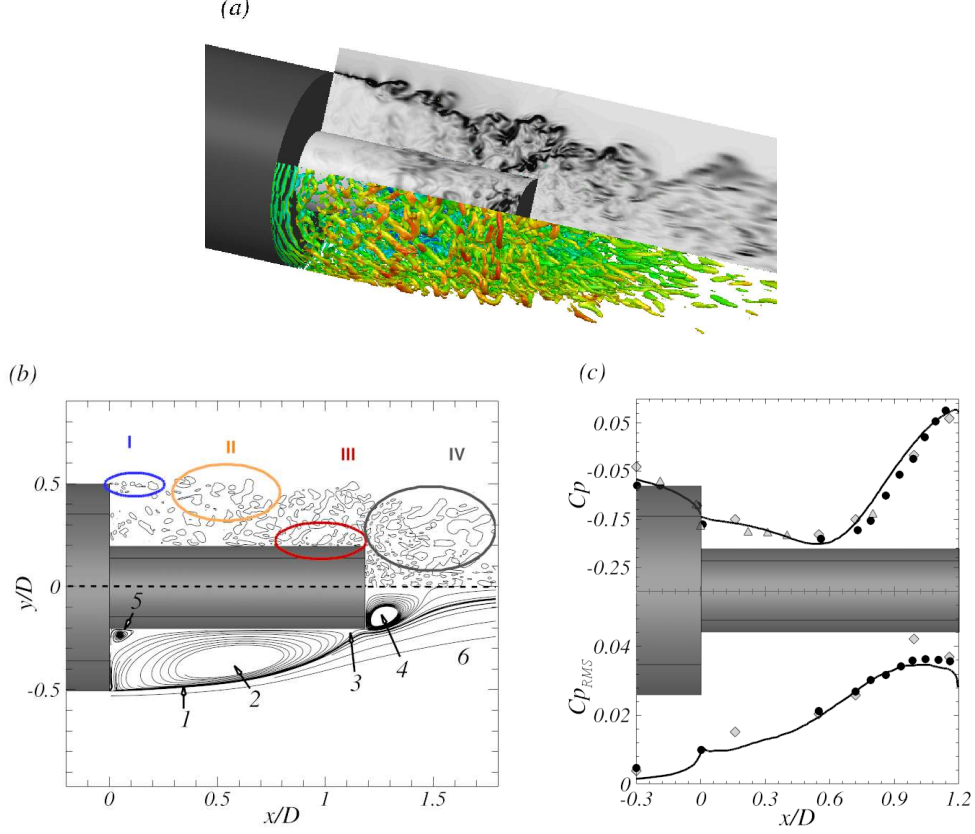


FIG. 5. (a) Isosurfaces of the normalised  $Q$ -criterion ( $QU_\infty^2/D^2 = 50$ ) coloured by the streamwise velocity and numerical pseudo-schlieren (gray scale) in a cut-off plane and on the skin of the emerging cylinder. (b) Figure adapted from Marié, Deck, and Weiss<sup>62</sup> - Mean (*bottom*) and instantaneous (*top*) organisation of the flow with mean streamlines (*bottom*) and isolines of  $QU_\infty^2/D^2 = 50$  (*top*) : 1. Mixing layer, 2. Recirculation zone, 3. Mean reattachment point, 4. Second recirculation zone, 5. Corner flow, 6. Turbulent wake - I. Kelvin-Helmholtz instabilities  $6 \leq St_D \leq 8$ , II. Flapping of the mixing layer  $0.07 \leq St_D \leq 0.1$ , III. Coherent structures impingement on the wall  $St_D \approx 0.6$ , IV. Vortex-Shedding  $St_D \approx 0.2$ . (c) Streamwise evolution of the mean (*top*) and  $RMS$  (*bottom*) pressure coefficient. (—) Zonal Detached Eddy Simulation (ZDES) from Weiss *et al.*<sup>9</sup> against experimental data from: ( $\diamond$ ) Deprés, Reijasse, and Dussauge<sup>11</sup> (kulites) ; ( $\triangle$ ) Deprés, Reijasse, and Dussauge<sup>11</sup> (steady tabs) ; ( $\bullet$ ) Meliga and Reijasse<sup>46</sup>

### III. SPATIAL ORGANISATION OF THE FLUCTUATING PRESSURE FIELD

This section aims at characterising the spatial organisation of the fluctuating pressure field around the backward facing step of finite length (figure 1). For that purpose, the instantaneous static pressure field within the computational volume shown in figure 1 was sampled through the ZDES numerical simulation.

The domain located behind the short cylinder in the wake is not sampled. This choice is motivated by the investigation by Deck and Thorigny<sup>8</sup> which concerned the same geometrical configuration as the present one with a major difference namely the inclusion of a supersonic jet located at the base of the short cylinder to represent the effect of a nozzle. In this case, the supersonic jet issuing from the nozzle is acting as a wall for the surrounding flow. Thus, in this former study, there is no secondary recirculation bubble in the wake downstream the short cylinder as in the present case. Comparing numerous relevant quantities for these two configurations (i.e. with and without jet), such as the streamwise evolution of the mean and fluctuating pressure coefficients or the characteristic frequencies resulting from spectral analyses (e.g. single-point and two-point spectra), no significant differences were observed. These results are fully in line with the experimental investigation by Deprés, Reijasse, and Dussauge<sup>11</sup> on this transonic axisymmetric step flow. Finally, this would suggest that the secondary recirculation is not of first importance in the flow dynamics given the a priori weak interactions with the primary recirculation zone.

The timestep of the simulation is equal to  $2 \mu\text{s}$ . However, the sampling is not performed at every timestep which would correspond to  $f_{\text{samp}} = 500 \text{ kHz}$ . In practice, the fluctuating quantities are stored every 5 timesteps leading to a sampling frequency of  $100 \text{ kHz}$ . This choice is supported by the fact that no energy is observed in the spectra anymore for frequencies higher than  $100 \text{ kHz}$  allowing to limit the data storage. Thus, the numerical sampling time is  $T_{\text{acq}} U_{\infty}/D = 476$  (i.e.  $T_{\text{acq}} = 0.2 \text{ s}$ ) and the sampling rate is  $f_{\text{samp}} = 100 \text{ kHz}$  in order to avoid any aliasing problem. The resulting database is composed of 20,000 snapshots with  $\Delta t U_{\infty}/D = 0.024$  representing 2 Terabytes of data storage.

As discussed in Sagaut and Deck<sup>64</sup> there is a contradictory aspect between the needs



for statistics and the constraints imposed by CFD. Indeed, to perform a statistical analysis in good conditions, the signal has to be well sampled on a sufficient duration because the spectral information needs to be averaged on many blocks to be statistically converged. In practice, unsteady signals issued from CFD are most often oversampled on a short duration (due to high CPU cost). Thus, a compromise has been found between the number of averaged blocks and the frequency resolution. The useful unsteady calculation of  $T.U_\infty/H = 1580$  which means that 200 ms of physical time have been simulated which is quite significant in term of CPU time consumed. Considering the fact that the main frequency of interest is here  $St_D = 0.2$  corresponding to 474 Hz (i.e. almost 0.002 s) we gather 100 periods of the shedding phenomenon. This sampling is already expensive. The timestep was equal to  $2 \mu\text{s}$  providing a minimal frequency that can be captured of 5 Hz. Considering a resolution for the spectrum of 60 Hz, we manage to average the spectral information over 23 blocks with a 50% -overlap using a Hamming window.

A Discrete Fourier Transform (DFT) is applied to this unsteady data set. Then the fluctuating pressure field distribution is investigated looking at the three-dimensional spectral content in the frequency and wavelength spaces. Another approach, namely a two-point correlation analysis as performed by Fuchs, Mercker, and Michel<sup>15</sup>, also reveals the spatial organisation of the fluctuating field.

### A. Energy distribution in Fourier space

First the frequency content of the separated region is investigated by means of a temporal Discrete Fourier Transform. The temporal Discrete Fourier Transform provides Fourier modes  $X(f)$  defined on a given frequency range. The spectral investigations are carried out on a frequency window ranging from 5 Hz to 100 kHz by steps of  $\Delta f = 60 \text{ Hz}$  ( $\Delta St_D \sim 0.025$ ). At each location in the computational volume (see figure 1), DFT is applied in order to compute the Power Spectral Density (PSD) of the local fluctuating static pressure  $p'(x, y, z, t) = p(x, y, z, t) - \overline{p(x, y, z)}$ . The one-sided PSD is here denoted  $G_{p'}(f)$  and reads:

$$\sigma^2 = \int_0^\infty G_{p'}(f) df = \int_{-\infty}^\infty f \cdot G_{p'}(f) d[\log(f)] \quad (2)$$

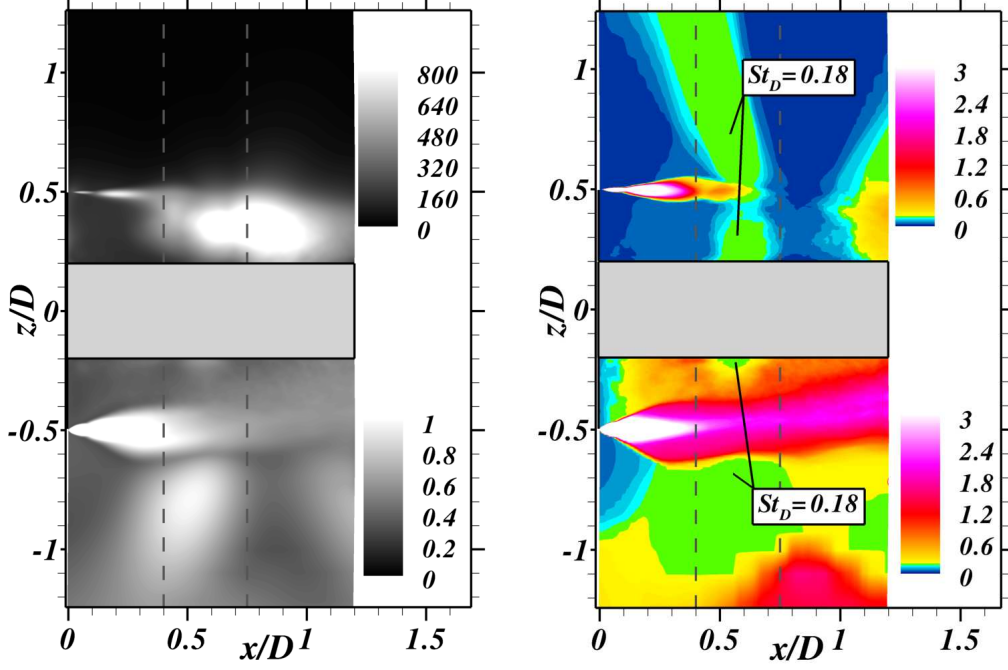


FIG. 6. Contours of the Power Spectral Density local maximum  $\max[G_{p'}(f)]$  in  $[\text{Pa}^2 \cdot \text{Hz}^{-1}]$  (*top, left*) against contours of the local maximum normalised PSD  $\max[fG_{p'}(f)/\sigma^2]$  (*bottom, left*) in plane  $(x/D, z/D)$ . Contours of the corresponding Strouhal numbers: (*top, right*)  $St_D(\max[G_{p'}(f)])$  against  $St_D(\max[fG_{p'}(f)/\sigma^2])$  (*bottom, right*).

Where  $\sigma$  is the standard deviation of the input signal.  $G_{p'}(f)$  indicates how power is distributed in the frequency domain. Once the PSD spectrum has been computed at each location, the local maximum value for  $G_{p'}(f)$  and the corresponding frequency  $f(\max[G_{p'}(f)])$  are extracted. Each leads to a set of  $N_i \times N_j \times N_k$  values averaged over the azimuth which is plotted in figure 6. The top two plots present the contours of  $\max[G_{p'}(f)]$  (grey scale) and  $St_D(\max[G_{p'}(f)])$  (coloured scale) the normalised frequency  $fD/U_\infty$  based on the diameter  $D$  and the free stream velocity  $U_\infty$ . The spectra are averaged in the homogeneous azimuthal direction. Thus, the graphic representation is reduced to plane  $(x, z)$ . In order to combine different levels of information, the contours of  $\max[fG_{p'}(f)/\sigma^2]$  (grey scale) and  $St_D(\max[fG_{p'}(f)/\sigma^2])$  (coloured scale) are depicted in figure 6 (*bottom*). While  $G_{p'}(f)$  provides the energetic level of each frequency,  $fG_{p'}(f)/\sigma^2$  returns the relative contribution of each frequency with respect to the total signal characterised by  $\sigma^2$  (see Eq. 2).

In order to illustrate the representativeness of the PSD peaks selected to plot two-dimensional maps of the PSD maxima, single-point spectra for the radial velocity  $u_r$  are

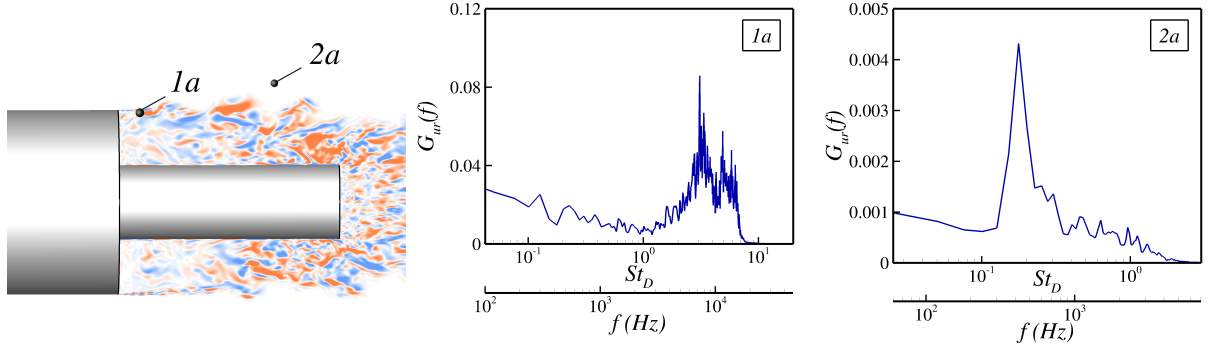


FIG. 7. Contour map of the streamwise vorticity sign (blue for negative and orange for positive) along the location of two sensors (left) used to plot single-point spectra at two characteristic locations inside (middle) and outside the mixing layer (right).

shown for two locations in figure 7. The definition of  $G_{u_r}(f)$  is similar to those of  $G_{p'}(f)$  in Eq 2. The numerical sensors are located inside and outside the mixing layer. Despite the two different frequency ranges which can be noticed, in both cases a broad band spectrum is observed along with a very prominent peak allowing an unambiguous selection of the maximum. The frequency content evolves a lot from point 1a to point 2a. Point 1a is located inside the mixing layer and exhibits two harmonics namely  $St_D = 3$  and 6 which correspond to typical high frequencies related to the vortex pairing phenomenon. The dimensionless frequency  $St_D = 0.18$  which is characteristic of the vortex shedding phenomenon can be distinguished. However, the shedding at point 1a is clearly overwhelmed by the shear layer process and is far less prominent than at point 2a which shows a clear peak at  $St_D = 0.18$ . This physical interpretation is supported by figure 6 (right).

The spectral map in figure 6 (*top, left*) indicates that the fluctuations with the highest levels are located on the second half of the emerging cylinder ( $0.55 \leq x/D \leq 1.0$ ), within the recirculation bubble ( $z/D \leq 0.5$ ). Besides, traces of intense fluctuations are captured in the area  $0 \leq x/D \leq 0.4$  and  $z/D = 0.5$ . The corresponding Strouhal numbers in this latter region are of the order of those expected in an early shear layer stage ( $St_D \geq 3.0$ ) as shown in figure 6 (*top, right*). The most significant unsteady feature of the flow appears to be related to the dimensionless frequency  $St_D = 0.18$ . The selected locus of this frequency is confined in a stripe-shaped area which lies from the emerging cylinder wall up to the free stream, passing through the mixing layer. This implies a very robust and dominant local

dynamics which seems to propagate in the radial direction. Such result corroborates those of Weiss *et al.*<sup>9</sup> who carried out a linear stability analysis on the present axisymmetric flow and put forward the absolutely unstable nature of the area  $0.35 \leq x/D \leq 0.75$ . This area is represented in grey dashed lines in figure 6. For  $x/D \geq 1.0$ , the wake dynamics feedback occurring at  $St_D = 0.18$  and  $St_D \sim 0.6$  can be interpreted as the signature of the classical vortex-shedding phenomenon found in the wake region<sup>(16,65)</sup>.

Considering figure 6 (*bottom, left*), a beam of high  $\max[fG_{p'}(f)/\sigma^2]$  values is observed in the mixing layer. This area highlights that the major part of the fluctuating energy arises from the Kelvin-Helmholtz instabilities. The corresponding Strouhal number map (figure 6 (*bottom, right*)) clearly depicts a linear spreading of the most amplified frequency which reflects the behaviour of a free mixing layer. In the second part of the cylinder extension, the inner part of the impinging shear layer presents a blurred distribution of the spectral content. In particular, the symmetry in the shear layer beam is broken at  $x/D \sim 0.3$  and  $z/D \sim -0.3$  with a wider frequency range dominated by the Strouhal number value  $St_D \geq 1.0$ . Such a breakdown in the symmetry may be the consequence of the intermittency of the reattachment point as shown by Weiss and Deck<sup>53</sup> resulting in an upstream and downstream convection of the impinging Kelvin-Helmholtz structures (Hudy, Naguib, and Humphreys<sup>59</sup>).

On top of this major source of turbulence, secondary patterns whose limits are indicated by two vertical dashed lines can be distinguished in the spectral map in figure 6 (*bottom, left*): one close to the wall in the absolutely unstable zone and two located in the outer part of the Kelvin-Helmholtz instability. According to figure 6 (*bottom, right*), those patterns correspond to the aforementioned  $St_D = 0.18$  dynamics. This suggests that the first half of the recirculation region is mainly driven by mechanisms of Kelvin-Helmholtz type whereas the far field dynamics is led by vortex-shedding periodicity.

It is distinguished an area with  $St_D \sim 0.07$  close to the separation point, spreading on the *outer* part of the shear layer. Such low frequency dynamics are ascribed to the flapping motion of the mixing layer<sup>12</sup>. Finally, the high  $St_D$  region in the far field (around  $z/D \sim -1$  and  $x/D \sim 0.9$ ) may be associated with turbulent noise radiating from the K-H instabilities.

## B. Azimuthal coherence distribution

As previously done by Fuchs, Mercker, and Michel<sup>15</sup> behind a circular disk, a modal decomposition in the azimuthal direction has been performed in order to quantify the correlation between two time signals in space. In the cylindrical coordinate system  $(r, \theta, x)$ , let  $\epsilon_1(r_1, \theta_1, x_1, t)$  be the signal at sensor 1 which will be considered as the reference input. Let  $\epsilon_2(r_2, \theta_2, x_2, t)$  be the second signal to be compared. Finally, a measure of the correlation between both signals by means of the coherence function is given by:

$$C(f, r_1, \Delta r, \theta_1, \Delta \theta, x_1, \Delta x) = \frac{G_{12}(f, r_1, \Delta r, \theta_1, \Delta \theta, x_1, \Delta x)}{\sqrt{G_1(f, r_1, \theta_1, x_1)G_2(f, r_2, \theta_2, x_2)}} \quad (3)$$

$$= (C_r + jC_i)(f, r_1, \Delta r, \theta_1, \Delta \theta, x_1, \Delta x) \quad (4)$$

Where  $G_1$  and  $G_2$  are the autospectrum of each signal and  $G_{12}$  is the corresponding interspectrum.  $\Delta r, \Delta \theta, \Delta x$  respectively define the radial, azimuthal and axial relative positions between the two sensors. Here the azimuthal direction is investigated, thus the computation of  $C$  reduces to pairs of sensors with  $r_1 = r_2 = r$  and  $x_1 = x_2 = x$ . Larchevêque *et al.*<sup>66</sup> emphasized that prior to physical interpretations one should determine the threshold beyond which the coherence  $\gamma$  becomes statistically significant. Such a threshold denoted  $\gamma_{99\%}$  depends on several parameters detailed in the literature<sup>67</sup>. On the basis of a Fisher law with a confidence interval of 99%, a level of  $\gamma^2$  stands for an effective correlation if  $\gamma > \gamma_{99\%}^2$  with :  $\gamma_{99\%}^2 \gtrsim 1 - 10^{\left(\frac{-4}{n_{dof}}\right)}$  according to Koopmans<sup>67</sup>. In the definition of  $\gamma_{99\%}^2$ ,  $n_{dof} = \frac{18}{11}n_b$  corresponds to the Welch's degrees of freedom Welch<sup>68</sup> with  $n_b$  the number of blocks over which the spectra are averaged. For the present case the estimation of such threshold returns  $\gamma > \gamma_{99\%}^2 \sim 0.40$  where  $\gamma = \|C_r + jC_i\|$ .

At this point it is important to be reminded of two major assumptions about the correlation function:

- Azimuthal homogeneity:  $C$  does not depend on the azimuthal position of the reference sensor (sensor 1) but only on the relative offset between the signals ( $\Delta \theta$ ).

- Azimuthal isotropy: statistically, the fluctuations should equally propagate in the positive and negative sense along the azimuthal direction. This assumption leads to  $C_i = 0$ .

Finally, the resulting  $C_r$  function is  $2\pi$ -periodic with respect to  $\Delta\theta$  and can be expressed thanks to a Fourier transform in azimuthal modes. In the present case:

$$C_r(f, \Delta\theta) = \sum_{m=0}^{\infty} C_{r,m}(f) \cos(m\Delta\theta) \quad (5)$$

where,  $C_{r,m}(f)$  denotes the relative contribution of mode  $m$  to the fluctuating energy at frequency  $f$  since  $\sum_m C_{r,m} = 1$ .

On the experimental side, Deprés, Reijasse, and Dussauge<sup>11</sup> carried out a similar decomposition. In Weiss *et al.*<sup>9</sup>, the study of the spatial organization of the energy for a given mode  $m$  was performed at the wall and not in the flow field as in the present work. By performing a coherence analysis in planes normal to the flow at three stations ( $x/D = 0; 0.12; 0.55$ ) on the wall of the emerging cylinder, the authors put forward that the highest levels of coherence for  $St_D \sim 0.2$  occur for an interval  $\Delta\theta = \pi$  between the pressure sensors. They deduced that this frequency is driven by the azimuthal mode  $m = 1$ .

In the hereby numerical simulation, this assumption is verified in figure 8 (*left*) in which the first azimuthal mode clearly dominates at  $St_D = 0.18$  along the  $x/D$  direction with a maximum value of the coherence value  $C_{r,m=1} = 0.8$  reached at  $x/D = 0.5$ . Figure 8 (*right*) shows the distribution at the wall of the real part of the coherence function for the azimuthal mode  $m = 1$ . The map illustrates that on the first half of the separated flow, the dynamics involving two diametrically opposite points ( $\Delta\theta = \pi$ ) is mainly governed by the shear layer flapping motion ( $St_D \sim 0.07$ ) while the second half exhibits high correlations around  $St_D \sim 0.2$ . It is worth noting the co-existence of both frequencies in the area  $0.3 \leq x/D \leq 0.75$  followed by the drop of  $C_{r,m=1}$  for  $St_D \sim 0.07$  to the benefit of  $St_D = 0.18$ . This suggests that the absolutely unstable zone may confine the effect of the flapping motion in the upstream region for  $m = 1$ .

In order to elucidate the origins of the  $C_{r,m=1}$  distribution at the wall, a coherence analysis in the radial direction has been performed for the main frequencies in figure 9. This latter depicts the spectral map ( $x/D, r/R$ ) of the first azimuthal mode for  $St_D = 0.07$  and

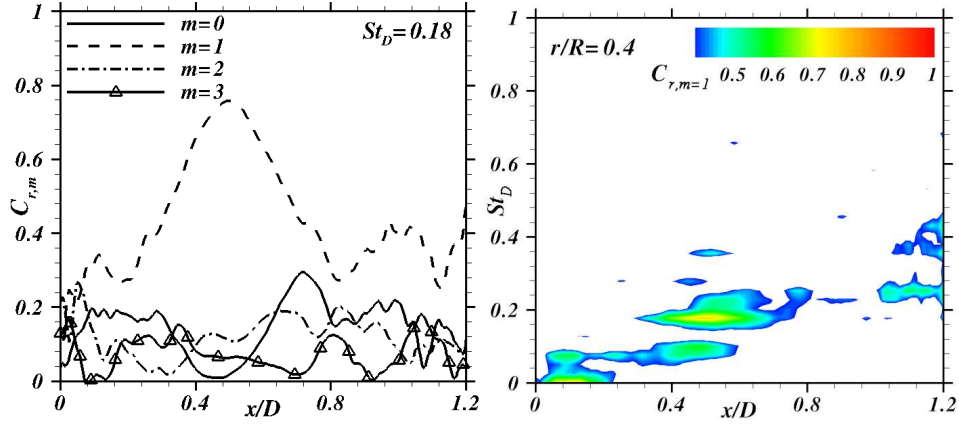


FIG. 8. (*left*) Evolution of the real part of the coherence function for the first four azimuthal modes for  $St_D = 0.18$  along the streamwise direction at the wall. (*right*) Spectral map ( $St_D, x/D$ ) of the first azimuthal pressure mode  $C_{r,m=1}$  at the wall ( $r/R = 0.4$ , with  $R$  the radius of the greatest cylinder).

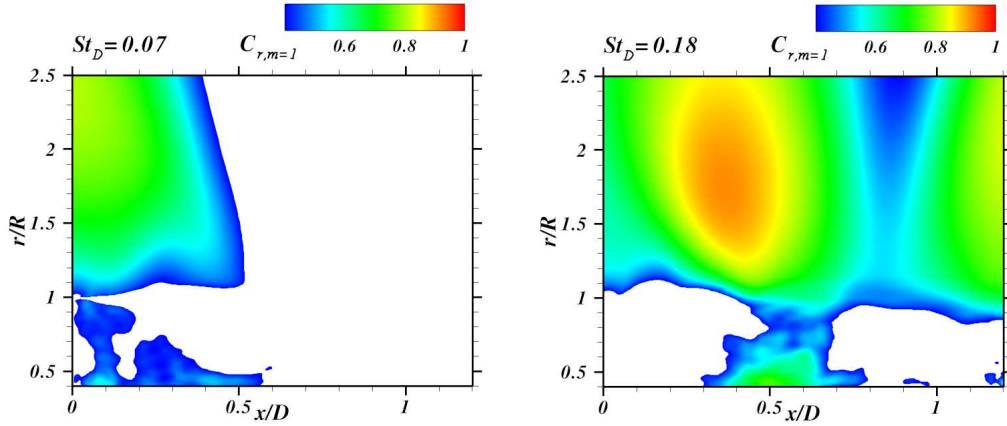


FIG. 9. Spectral map of the first azimuthal pressure mode  $C_{r,m=1}$  along the streamwise ( $x/D$ ) and radial ( $r/R$ ) directions for Strouhal numbers  $St_D = 0.07$  (*left*) and  $St_D = 0.18$  (*right*).

$St_D = 0.18$ . As in figure 8 (*right*), only the first half of the separated flow features high correlation levels at  $St_D = 0.07$ . Nevertheless, an area of high correlation is found in the range  $0 \leq x/D \leq 0.5$  above the mixing layer ( $r/R \sim 1$ ), where the flow dynamics is not disturbed by any turbulent fluctuations. It is also worth reporting some significant coherence areas underneath the mixing layer. This suggests that the flapping dynamics constitutes a robust feature of the turbulent shear layer and significantly affect the organisation of the recirculation area.

High correlation levels in the mixing layer also occur in the interval  $0.3 \leq x/D \leq 0.8$  for  $St_D = 0.18$  as shown in figure 9 (*right*). One should remark that the specific position  $x/D \sim 0.3$  corresponds to the locus where the Kelvin-Helmholtz fluctuations become less intense according to figure 6 (*left*). Finally, by the end of the emerging cylinder, the feedback of the wake vortex-shedding is captured as it was mentioned previously.

In this subsection, it has been put forward that the unsteady dynamics is governed by the first azimuthal mode  $m = 1$  which implies that fluctuations at two diametrically opposed points are paired in time. Then, the spatial distribution of the most excited Strouhal numbers is typical of the flapping motion of the mixing layer ( $St_D = 0.07$ ). This dynamics dominates in the first part of the emergence before being overwhelmed by the vortex-shedding phenomenon ( $St_D = 0.18$ ). The dynamics of the flow phenomena related to these two frequencies appears to be stronger in the free stream.

More globally, the three-dimensional fluctuating field has been characterised both in the Fourier space and in terms of azimuthal coherence. This analysis provides a detailed profile of the unsteady axisymmetric backward facing step flow. Yet, a further insight is required in order to shed light on the three-dimensional spatial organisation of each characteristic frequency of the fluctuating field. Practically, such an analysis is usually performed by decomposing the flow structures into modes. In this study, the Fourier mode decomposition method is used. Results are discussed in the next section in which a comparison with the recent Dynamic Mode Decomposition method is also performed, to cross-check the first analysis.

## IV. MODAL DECOMPOSITION OF THE THREE-DIMENSIONAL PRESSURE FIELD

### A. Fourier modes

It is reminded that the temporal Discrete Fourier Transform provides Fourier modes  $X(f)$  defined on a given frequency range and that the spectral investigations are carried out on a frequency window ranging from 5 Hz to 100 kHz by steps of  $\Delta f = 60$  Hz ( $\Delta St_D \sim 0.025$ ). The previous analysis focused on the Power Spectral Density  $G_{p'}(f)$  of each Fourier mode, i.e. the square modulus of  $X(f)$  over the integration period for each frequency band  $\Delta f$ .



In this section, each Fourier mode is considered in its complex form at each point in the computational volume (shown in figure 1). The complex Fourier modes associated with the four characteristic frequencies identified in the preliminary investigations ( $St_D = 0.07, 0.18, 0.60, 6.21 (\pm 0.025)$ ) were extracted. The specific value of the dimensionless frequency  $St_D = 6.21$  has been selected to illustrate the shape of the mode related to the characteristic frequency observed in the early stages of the shear layer. This value decreases downstream in the mixing layer far from the separation as shown in Weiss and Deck<sup>53</sup>. In the early stages of the mixing layer the characteristic high frequencies are ranging from  $St_D = 5$  and  $St_D = 8$ . Both the Fourier and DMD modes have similar shapes in this range. Modes are represented for each characteristic frequency range namely  $St_D = 0.07$  for the flapping phenomenon,  $St_D = 0.18$  for the shedding phenomenon,  $St_D = 0.6$  for the oscillation of the reattachment point of the recirculation bubble along the extension,  $St_D = 6.21$  for the K-H instability.

Weiss *et al.*<sup>9</sup> showed thanks to a linear stability analysis that the axisymmetric body dynamics is led by a significant unstable area centered around  $x/D \approx 0.55$  suggesting a global instability mechanism. Let us be reminded that in that case, the flow can behave as an oscillator and imposes its own dynamics. Self-sustained oscillations are observed which are characterised by a well-defined frequency  $f_0$  (or wavelength  $\lambda_0$ ). This behaviour is clearly educed in figure 8 showing the spatial distribution of its energy and the antisymmetric nature of the corresponding mode has been investigated by the azimuthal Fourier transform of the interspectrum of pressure fluctuations at frequency  $St_D = 0.18$  (figure 9).

As an additional way to investigate this major property of the flow, one can also consider directly the spatial distribution of the local single-point time Fourier transform. As a preliminary example, let us consider the complex exponential mode of pure harmonic behavior *i.e.* characterised by its frequency  $f_0$  (or wave length  $\lambda_0$ )  $Ae^{2j\pi f_0 t}$  (or  $Ae^{2j\pi \frac{\lambda}{\lambda_0}}$ ) which has a constant modulus  $A$ .

Figure 10 reminds that there are different ways of considering such a signal by either its real  $\mathcal{R}(\bullet)$  and imaginary part  $\mathcal{I}(\bullet)$  or its amplitude and phase  $\phi = \text{Atan}\left(\frac{\mathcal{I}(\bullet)}{\mathcal{R}(\bullet)}\right)$ . To get further insight into the spatial organisation of the intrinsic dynamics of the flow, the complex Fourier transform  $X(f)$  of the fluctuating pressure field  $p'(t)$  is analysed.

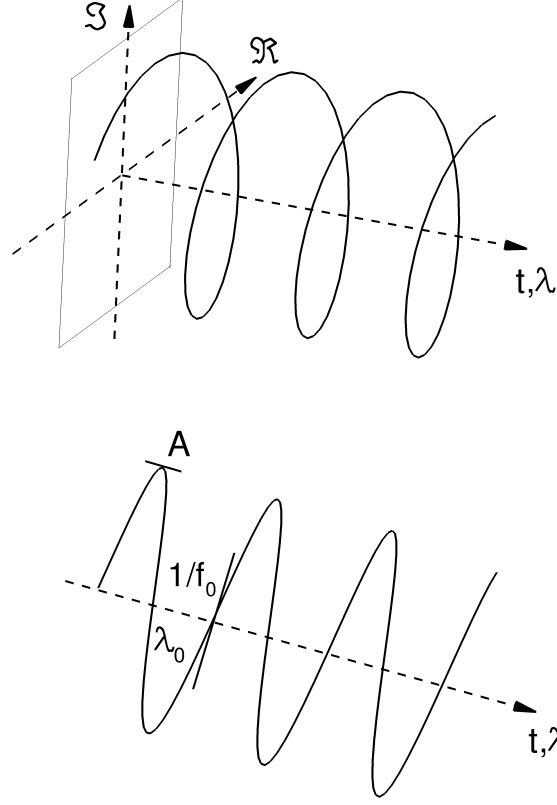


FIG. 10. Different depictions of the model  $Ae^{2j\pi f_0 t}$  (or  $Ae^{2j\pi \frac{\lambda}{\lambda_0}}$ ).

First, figure 11 displays the imaginary part of the Fourier mode ( $\mathcal{I}(X_{St_D=cst}(f))$ ) on each grid point for a set of selected frequencies of interest. Contours are normalised by the sampling frequency  $f_{samp}$  to directly obtain a data representation in a physical unit, *i.e.* Pascals (Pa). The selected computational volume allows to extract half of a wavelength in the streamwise direction for this specific Strouhal number. As expected, considering the spatial distribution of the observed patterns, the wavelength decreases as the Strouhal number grows. Besides, contours of  $\mathcal{S}[X_{St_D=cst}(f)]$  at  $St_D = 0.18$  clearly exhibit a sequence of diametrically opposed positive and negative patterns with alternating orientation in the direction transverse to the flow. One can note that both experimentally and numerically, the flow is likely to adopt one single orientation due to local perturbations (surface roughness, numerical methods).

In contrast to the fully antisymmetric behaviour observed at  $St_D = 0.18$ , a large ax-

isymmetric pattern located on the second half of the emerging cylinder is evidenced at  $St_D = 0.07$ . Such a difference is consistent with the results of Deck and Thorigny<sup>8</sup> who unveiled that the shear layer flapping motion around  $St_D = 0.07$  is associated with the azimuthal mode  $m = 0$  while the vortex shedding is related to the antisymmetric mode  $m = 1$ . Then, two diametrically opposed zones are observed close to the separation edge. This spatial distribution corroborates the results of section III B. In this section, the area  $0 \leq x/D < 0.55$  is characterised by a high coherence level for the first azimuthal mode (see figure 9) which rapidly falls to low levels of  $C_r$  for  $x/D \geq 0.55$ ).

The spatial distribution of the Fourier mode related to  $St_D = 0.60$  is similar to that of  $St_D = 0.18$  with a shorter streamwise wavelength. One should note, that for this frequency range, the pressure contours are extended in the radial direction and slightly tilted downstream. This feature may be related to the acoustic propagation and the tilting to the advection effect<sup>66</sup>.

The isosurfaces of  $\mathcal{I}[X(f)] \cdot f_{smp} = \pm 200$  [Pa] at  $St_D = 6.21$  in figure 11 (*bottom, right*) clearly show the presence of toroidal structures that are convected along the direction of the shear layer and remain well organised as a sequence of alternated positive and negative high fluctuating pressure zones. Such a distribution is characteristic of the Kelvin-Helmholtz convective instabilities as discussed by Huerre and Rossi<sup>63</sup>.

To further investigate the dynamics associated to a given frequency  $St_{cs}$ , the focus is put on the inverse Fourier Transform of the pressure Fourier mode. Indeed, the inverse Discrete Fourier Transform states that the initial discrete pressure signal  $p'(t_i)$  ( $i = 1, \dots, N$ ) can be rebuilt from all the Fourier modes  $(X(f_k))_{f_k = \frac{k}{N}f_{smp}, [k=0, \dots, N-1]}$ .

Due to the Hermitian symmetry of the discrete Fourier transform  $X(f_k) = X^*(f_{N-k})$ , the reconstructed fluctuating pressure field  $p'_r(t_i)$  is real-valued:

$$p'_r(t_i) = \frac{1}{N} \sum_{k=0}^{N-1} X(f_k) \cdot e^{2\pi j \frac{k}{N} t_i} \quad (6)$$

Then, following this reconstruction step, only one mode for each characteristic frequency of the flow dynamics is selected. Let  $St_{cs}$  be the characteristic selected frequency,  $p'_r(t_i)|_{St_k=St_{cs}} = X(f_k)|_{St_k=St_{cs}} \cdot e^{2\pi j \frac{k}{N} t_i|_{St_k=St_{cs}}}$  is complex-valued while  $p'_r(t_i)$  defined by all

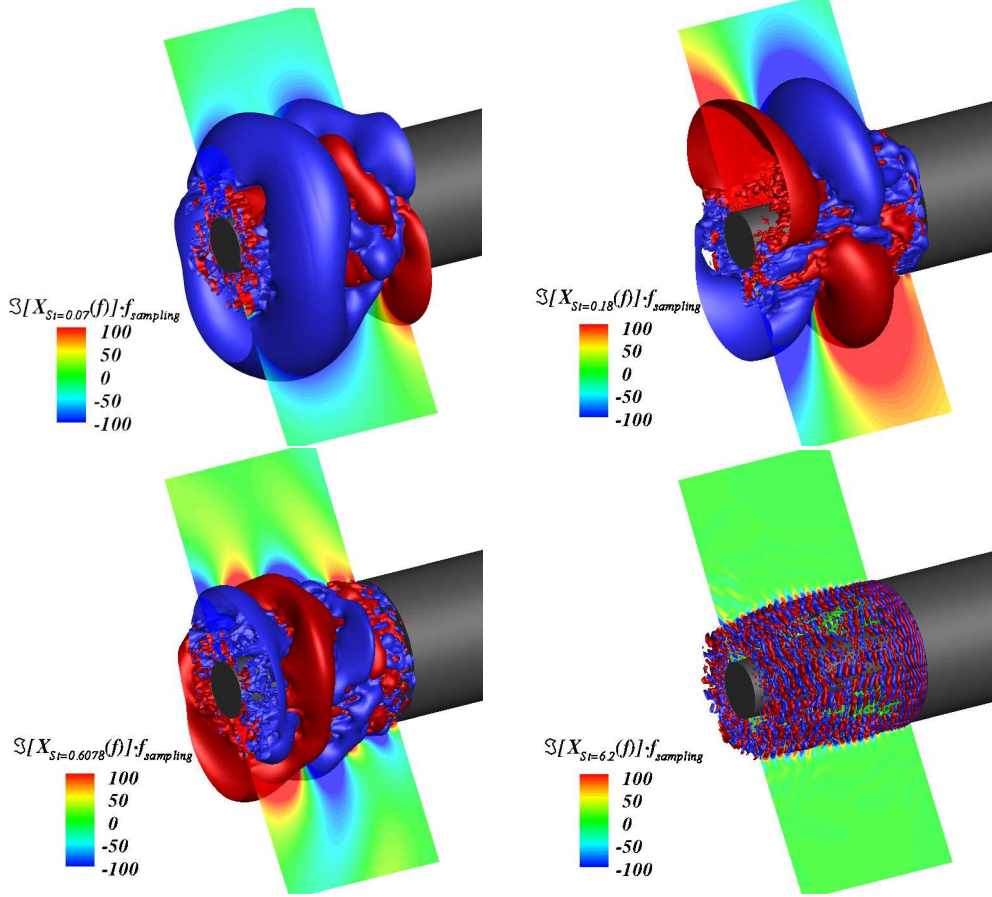


FIG. 11. Contours of  $\Im(X(f)) \cdot f_{sampling}$  [Pa] and isosurfaces  $\Im(X(f)) \cdot f_{sampling} = 200$  (red) and  $\Im(X(f)) \cdot f_{sampling} = -200$  (blue) of the Fourier modes associated with (from *top left* to *bottom right*)  $St_D = 0.07$ ,  $St_D = 0.18$ ,  $St_D = 0.60$  and  $St_D = 6.21$  (the flow goes from right to left).

modes (see Eq 6) is real-valued.

The physical interpretation of  $\Im(X(f_k)|_{St_k=St_{cs}} \cdot e^{2\pi j \frac{k}{N} t_i}|_{St_k=St_{cs}})$  is not commonly used but in practice this quantity is simply related to the time derivative of  $p'(t_i)^{69}$  which is relevant to evidence a large scale unsteady process.

To complete the representation of the mode both the real and imaginary parts of the DMD modes as well as the corresponding phase are plotted (see figures 14,15,16).

Figure 12 shows four snapshots of the inverse Fourier mode dynamics associated with  $St_D = 0.18$  with a time interval  $\Delta t = T/6|_{St=0.18}$  between each other so that half of a period

is reproduced. Organisation at  $t = T_0$  has been discussed above and is consistent with the conclusion of the spectral study in the wave number space which evidenced the dominance of  $\lambda_\theta = \pi D/2$ . Snapshot at time  $T_0 + T/6|_{St=0.18}$  illustrates the convection of the large scale pairs at the extremity of the emerging cylinder towards the wake region. This is coupled with a slight convection downstream close to  $D/4$  and a growth in size of the upstream negative fluctuating pressure pattern (represented in blue). Snapshot  $T_0 + 2T/6|_{St=0.18}$  depicts the appearance of an extra pair of structures close to the separation edge while the initial ones keep convecting downstream. The last figure exhibits a switch in the organisation of the first snapshot since the exponential term in equation 6 provides the periodic aspect of the dynamics and bears the intrinsic pulsation of  $St_D = 0.18$ .

It is remarked that the most amplified pressure patterns (snapshots  $T_0$  and  $T_0 + T/2|_{St=0.18}$ ) occur at specific locations along  $x$ . The first one is located in the absolutely unstable area ( $0.35 \leq x/D \leq 0.75$ ) identified by Weiss *et al.*<sup>9</sup> while the second one is located by the edge of the emergence ( $0.75 \leq x/D \leq 1.2$ ). This suggests that the dynamics in the radial direction is mostly driven by the intrinsic pulsations of the absolutely unstable region. Periodically, large scale coherent structures emerge from that region. As they convect downstream and reach the edge of the small cylinder, they are likely to induce large scale vortices, rotating in the streamwise plane, due to the radial pressure gradients and constitute the von Kármán alley in the wake region.

In this paragraph, the spatial distribution of the Fourier mode is investigated by considering the phase  $\phi(X(f)) = \text{atan}[\Im(X(f))/\Re(X(f))]$  which therefore provides the location of the Fourier mode in the complex plane. The regions of positive and negative values for the phase  $\phi(X(f))$  exhibit a helical shape for  $St_D = 0.18$ . This is emphasized in figure 13 with the isosurfaces  $\phi(X(f)) = \pm 0.02$  which bound the two different areas. Direction  $x$  in the figure was stretched for graphical purpose. Such a spatial structure of the pressure fluctuations related to the vortex-shedding is consistent with the experimental observations of Taneda<sup>14</sup> and Berger, Scholz, and Schumm<sup>17</sup> who put forward the assumption that the flow past a sphere might adopt a helical organisation. Monkewitz<sup>16</sup> showed that the preferred instability mode in the axisymmetric wake is a spiral which was explicitly evidenced by Weickgenannt and Monkewitz<sup>19</sup> on an axisymmetric bluff body wake at  $Re_D = 3 \times 10^4$  with a representation of the phase-locked velocity. To the authors' best knowledge, this helical mode is highlighted for the first time in physical space thanks to a Fourier analysis of the

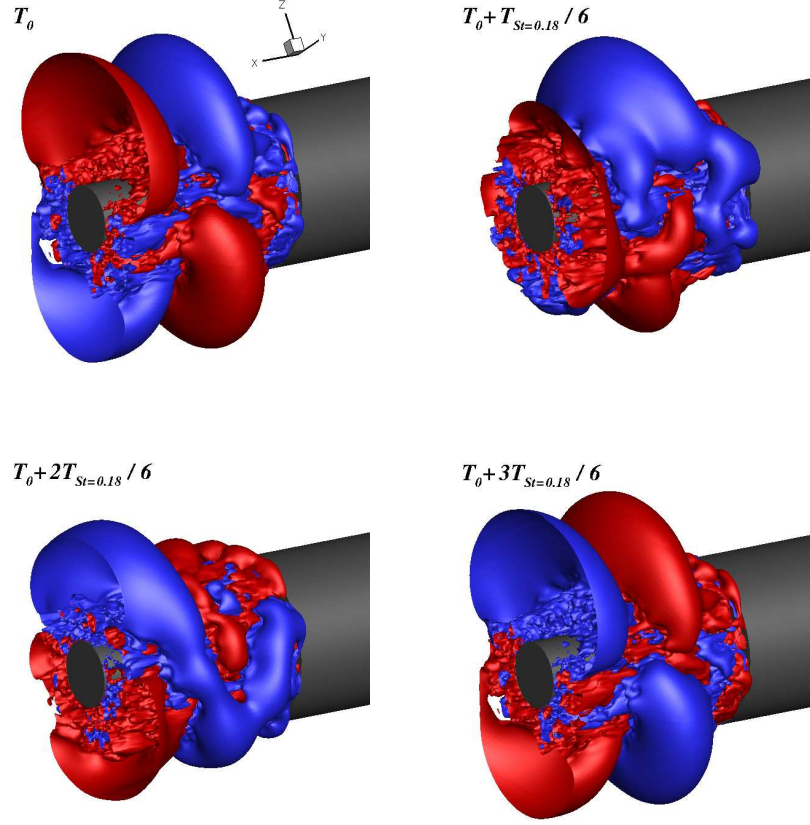


FIG. 12. Visualisation of the computed inverse Fourier mode dynamics (imaginary part) associated with  $St_D = 0.18$ . The values of the two isosurfaces are  $\Im(X(f)) \cdot f_{samp} = 200$  (red) and  $\Im(X(f)) \cdot f_{samp} = -200$  (blue). Each picture is  $\Delta t = T/6|_{St=0.18}$  apart from top left to bottom right (the flow goes from right to left).

fully three-dimensional fluctuating field. Besides, the coexistence of absolute helical ( $m=1$ ) unstable global modes within the recirculation region and convectively unstable shear layer modes corroborates the results of Sandberg and Fasel<sup>10</sup> on supersonic axisymmetric wakes. Since the large scale helical structure is captured at the early separation stage of the flow, it suggests that the spiral organisation exposed by Monkewitz<sup>16</sup> derives from the convergence of the hereby helix, as it convects downstream, towards a location on the axisymmetric axis. The data provided in this study does not allow to confirm such an assumption since the computational volume of acquisition is restricted to the recirculation area. In addition,

the presence of the emerging cylinder may certainly affect the evolution of the spiral radius compared to the case of a single axisymmetric bluff-body.

For bluff-body flows the analogy between a low-Reynolds (laminar and incompressible) configuration, such as the cylinder plate or sphere case<sup>6,20,70–72</sup>, and higher Reynolds number (and high subsonic  $M_\infty = 0.7$ ) is hardly comparable. Indeed, the flow around a sphere at  $Re = 300$  is the seat of a self-sustained instability around the Strouhal number of 0.135. This dynamics generates vortex-shedding formed by coherent structures such as hairpins. The higher Reynolds number dynamics has different characteristics. Although a fully turbulent flow may also be the site of a global instability (dynamics temporally self-sustained), like its laminar counterpart (see Weiss *et al.*<sup>9</sup>), the spatial development of these instabilities is generally very different. The reason is that there are also highly unstable convective instabilities (and sensitive to different environmental forcings) at high Reynolds numbers that interact and blend with the global instabilities generating complex structures formed by an aggregate of smaller structures. The helical structure described in this paper is obviously not a coherent structure as can be the hairpin at low Reynolds number but rather a cluster of spatio-temporally correlated structures. The preexistence of coherent structures upstream can further complicate the spatio-temporal dynamics.

The rapid phase variation of the azimuthal Fourier mode  $m = 1$  observed at  $x/D \approx 0.9$  in figure 13 is indeed quite brutal because it corresponds to a sudden change in dynamics. The beginning of the emergence ( $x/D < 0.5$ ) corresponds to the development of the vortex structures attached to the mean shear-layer and driven mainly by the mean local vorticity thickness  $\delta_\omega(x)$ . Around  $x/D \sim 0.5$ , the structures attached to the mean shear-layer are shedded, the coherent structures no longer follow the mean shear-line, this is the vortex-shedding phenomenon. The global motion is then mainly helical (with an azimuthal wave number  $m = 1$ , see<sup>9</sup>). On the other hand, the existence of an absolute (global) instability in the zone<sup>9</sup> of an azimuthal wave number  $m = 1$  represents the presence of a helical dynamics which drives the flow downstream.

As for the validity of a linear stability analysis for a turbulent flow, it has indeed been carried out for a long time with sometimes a real success but without real theoretical justification. Recent studies are beginning to better lay the theoretical framework of such an analysis<sup>73–75</sup>.

In the study by Statnikov, Meinke, and Schröder<sup>30</sup> a cross-flapping motion of the shear layer is observed at  $St_D \simeq 0.2$ , triggered by antisymmetric vortex shedding. The present results firstly introduced in Pain, Weiss, and Deck<sup>26</sup> show the same thing. The main differences lie in the interpretation of the dynamics of the antisymmetric character. In both simulations, there are hairpins, lambda vortices, stripes and structures on the scales of the order of the vorticity thickness of the shear profile. These structures do not play a direct role in the antisymmetric dynamics at  $St_D \simeq 0.2$ . A major difference lies in the jet of the nozzle which is included in the work of Statnikov, Meinke, and Schröder<sup>30</sup> and not in the present study. Taking this jet into account can significantly alter the overall dynamics of the wake and could lead to different conclusions. However, it is important to note, that the presence of the jet does not alter the existence of a  $St_D \simeq 0.2$  dynamics that originates in an absolutely unstable zone around the extension and not in the near wake (Weiss *et al.*<sup>9</sup>). The near wake, which is of convective (and not absolute) nature, is then forced by this temporally self-sustaining dynamics and develops convectively unstable instabilities. The latter are strongly influenced by the local topology of the flow and therefore by the presence or absence of the jet.

As it was mentioned above, the helix seems to feature an anti-clockwise oriented rotation when facing the flow. Although here the helix pitch is not constant along  $x$  due to the stretching of the  $x$  direction, it can be measured that the isosurface  $\phi(X(f)) = 0.02$  covers an angle  $\pi$  across a distance  $l_\pi \sim 0.9D$  leading to an approximated pitch  $\alpha \sim 0.29D$  [m.rad<sup>-1</sup>]. The complete rotation is thus expected to be performed for  $l_{2\pi} \sim 1.8D$ . This is of the order of the absolute wave length  $\lambda_0$  from Weiss *et al.*<sup>9</sup> who derived the stream-wise evolution of  $\lambda_0$  by means of a linear stability analysis and obtained  $\lambda_0 = 2.05D$  in the absolutely unstable region. Even though Weickgenannt and Monkewitz<sup>19</sup> investigated the axisymmetric bluff body wake in the Reynolds number range  $3 \times 10^3 \leq Re_D \leq 5 \times 10^4$ , the authors did not report the effect of  $Re_D$  on the geometrical characteristics of the spiral. Yet, from the downstream evolution of the phase-locked velocity  $\langle V_x \rangle / V_\infty$ <sup>19</sup>, the approximated spiral pitch is  $\alpha_{\text{bluff-body}} \sim 0.64D$  [m.rad<sup>-1</sup>] at  $Re_D = 3 \times 10^4$ . This conjectures that the higher the Reynolds number, the lower the pitch and the more spin the spiral gains. Armaly *et al.*<sup>7</sup> experimentally evidenced on a three-dimensional backward facing step that the length of the recirculation bubble decays as the Reynolds number increases. This would support the previous assumption that the helical dynamics is compressed to a smaller volume as the



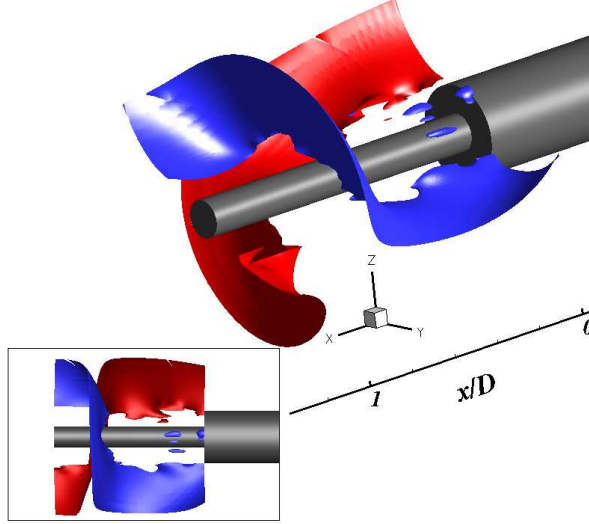


FIG. 13. Isosurfaces  $\phi(X(f)) = \pm 0.02$  of the phase  $\phi(X(f)) = \text{atan}(\Im(X(f))/\Re(X(f)))$  of the Fourier mode associated with  $St_D = 0.18$  (the flow goes from right to left).

reattaching length decreases.

To conclude, the spatial organisation associated with the main frequencies identified in section III namely  $St_D$  has been evidenced. The analysis of the imaginary part of the Fourier modes highlighted the antisymmetric nature of the fluctuating pressure 3D distribution associated with  $St_D = 0.18$  as opposed to axisymmetric structures for  $St_D = 0.07$ . A temporal reconstruction of the Fourier mode associated to  $St_D = 0.18$  has been performed in order to investigate the radial dynamics of the vortex-shedding phenomenon. Finally, the visualisation of the phase of  $X(f)|_{St=0.18}$  put forward the helical nature of that mode.

## B. Dynamic modes

In the diversity of modal decomposition methods, the Dynamic Mode Decomposition (DMD) derived by Rowley *et al.*<sup>76</sup> and Schmid<sup>77</sup> has been used in this section with the view to support the results of the previous section. This method relies on the spectral analysis of a linear operator called the Koopman operator<sup>76</sup>. Each dynamic mode is characterised by its own frequency. As such, this method is a well-adapted tool to compare with the above results. Chen, Tu, and Rowley<sup>78</sup> have mathematically shown that DMD on mean-subtracted input data is equivalent to the temporal Discrete Fourier Transform. The aim of this section is to apply the Dynamic Mode Decomposition on such an input data contest

with the view to cross-check the spatial distribution that has been derived above with an alternative approach.

The main purpose of this study is to show that the nonlinear dynamics of a flow around an axisymmetric backward-facing step with downstream cylinder has a large-scale helical structure as well as a hierarchy of structures at intermediate scales. To best of the authors' knowledge, the illustration of such a result by two different methods constitutes a novelty. Concerning the equivalence between the temporal discrete Fourier transform and the DMD, there are several works giving a framework to this equivalence. Historically, Rowley *et al.*<sup>76</sup> and Schmid<sup>77</sup> proposed the DMD which has the advantage to be a frequency modal decomposition easily accessible. Appendix A has been added for a detailed description of this method. The advantage of the DMD, relative to other frequency decomposition such as for example Fourier decomposition, is to better grasp the real physical mechanisms, in particular for transient or non-equilibrium phenomena. The DMD can be used with both experimental and numerical data. The main constraint is to have access to sufficiently time-resolved data. One important difference between for example another decomposition like POD and the DMD algorithm is that the mean is not first subtracted for DMD. This is important to note, as it can be shown that subtracting the mean before applying DMD gives results identical to a temporal discrete Fourier transform Chen, Tu, and Rowley<sup>79</sup>, if the equation  $y_{k+1} = Ay_k$ ,  $k = 1, \dots, m$  (see Appendix A) is satisfied exactly (e.g., if the first  $m$  snapshots are linearly independent). Generally, this equivalence is obtained when the flow is statistically stationary.

In our case, although the flow is fully turbulent, the latter is massively separated, which *a priori* does not allow to be certain to be "statistically stationary". Indeed, there is in particular a self-sustained dynamic that is weakly dependent on the scales characteristic of turbulence<sup>9</sup>. In this type of regime, the DMD is well posed and not totally equivalent to a DFT, so it is interesting to cross methods to confirm (or deny) the robustness of physical mechanisms observed (here the large-scale helical movement).

Table II sums up the differences between Fourier and DMD approaches in terms of input and output data as well as 3D representations.

Starting from the same dataset containing the fluctuating signal at each point of a given

volume, the Fourier analysis focuses on a sole variable (e.g. the pressure  $p$ ) whereas the DMD needs multiple variables depending on the definition of the scalar product Chen, Tu, and Rowley<sup>78</sup>, Aubard, Robinet, and Gloerfelt<sup>80</sup>. Then, a major difference lies in the need for a matrix inversion to obtain the DMD spectrum from the whole computational domain  $\Omega$  while the space-time representation of the spectral content using a Fourier analysis can be obtained computing one PSD spectrum for each point in  $\Omega$ . The  $N_{ijk}$  operations required to calculate the PSD spectra are easy to parallelize. At the opposite, DMD operations Rowley *et al.*<sup>76</sup>, Schmid<sup>77</sup>, Schmid *et al.*<sup>81</sup> involving matrix inversion needing a rapidly increasing memory storage are far more expensive.

A summary of the computational costs required for the computation of the 3D Fourier and DMD modes is gathered in Table III.

Indeed, Table III shows an estimation of the needed CPU time for the DMD based on the same dataset as for the Fourier analysis. Such a post-processing would lead to 1,200 days on a single processor. Even a massive parallelization of the DMD algorithm distributed over 2,400 cores and taking  $O(400)$  h CPU time as the one performed by Statnikov, Meinke, and Schröder<sup>30</sup> allows only to treat 512 snapshots (requiring 0.65 Gb of storage) and containing  $N_{ijk} = 16.5 \times 10^6$  points.

Thus, such computational costs justify the use of both a coarser mesh and a reduced snapshot dataset which clearly enables a drastic reduction in CPU time and memory cost. A critical assessment of Fourier and Dynamic modes can be done. In fact, a major advantage of the Fourier analysis lies in the opportunity to use the complete available dataset which ensures to get access to all the spectral content with the sole limitation imposed by the total duration of the signal and the sampling frequency and the Nyquist-Shannon criterion, consequently.

In the present study, the input raw numerical data for this modal analysis consists in a set of  $N = 10,000$  snapshots of the 3D fluctuating pressure field sampled from the initial data set used in the previous section ( $T_{acq} U_\infty / D = 476$  i.e.  $T_{acq} = 200$  ms). The sampling frequency of the DMD modes is 50 kHz which has to be compared to the one used for the Fourier modes which is higher and equal to 100 kHz. Besides, the dynamic modes were computed on a coarser grid consisting of  $35 \times 23 \times 121$  points. This coarser mesh derived

TABLE II. Sketch summarising the main differences between PSD and DMD approaches.

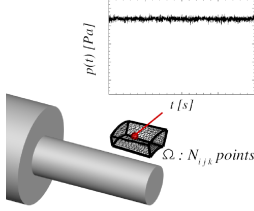
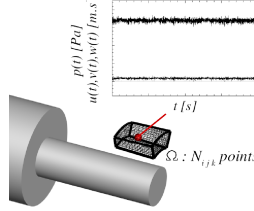
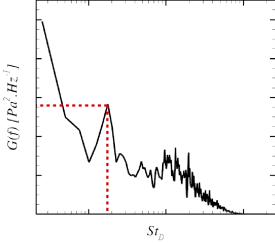
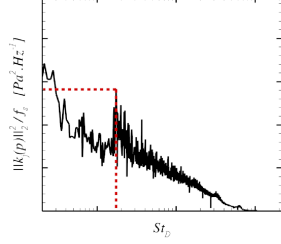
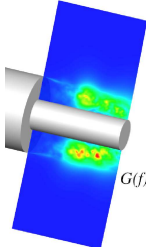
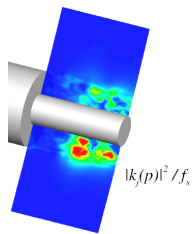
	Fourier PSD	DMD
<b>I :</b>	fluctuating signal at one point (one variable : pressure $p$ )	fluctuating signal at one point (multi-variables : depends on the scalar product)
		
<b>O :</b>	one PSD spectrum for each point in $\Omega$	one DMD spectrum for the whole computational domain $\Omega$
		
<b>3D :</b>	requires $N_{ijk}$ PSD operations	1 3D DMD operation
		

TABLE III. CPU time and storage requirements for both the DMD and Fourier analysis on a single core.

	$N_{ijk}$ [points]	Storage [Gb]	$N$ [snapshots]	$T_{TOTAL}$ [h]
present DMD	$0.1 \times 10^6$	4	10,000	$O(88)$
DMD with Fourier analysis requirements	$4.5 \times 10^6$	2,000	20,000	$O(2.8 \times 10^4)$
present Fourier analysis	$4.5 \times 10^6$	2,000	20,000	$O(20)$

from the initial one, exposed in section II A, using space modulo in the three directions. The aim for such reductions in both the temporal and space parameters is to reduce the CPU time involved. The Arnoldi algorithm for the computation of the dynamic modes was provided in an in-house sequential code. It consists in two main steps that are first the computation of a so-called Companion matrix and finally the resolution of the eigenproblem associated with that matrix.

Each of the eigenvalues computed is associated with one dynamic mode  $K_j$  whose frequency is given by  $f_j = \Im(\log(\lambda_j))/2\pi\Delta t$  where  $\lambda_j$  is the eigenvalue associated with  $K_j$  and  $\Delta t$  is the time step between the snapshots ( $\Delta t = T_{acq}/N$ ). As a comparison with the Fourier modes, contours of the real part, the imaginary part and the phase of the dynamic modes associated with  $St_D = 0.07; 0.18; 0.60; 6.21$  are shown in figure 14. In particular, the phase plotted for DMD modes shows a continuous helical shape.

The global spatial distribution provided by the dynamic modes is consistent with those of the Fourier method as the wavelengths fit well with each other. Although the dynamic mode associated with  $St_D = 0.07$  is axisymmetric and is in agreement with contours of  $\Im(X(f))|_{St=0.07}$ , the sequence of the positive and negative pressure patterns is inverted compared to the Fourier results. Moreover,  $\Im(K_j)$  at  $St_D = 6.21$  exhibits significantly less coherent structures than  $\Im(X(f))|_{St=6.21}$  which is the consequence of the coarser grid.

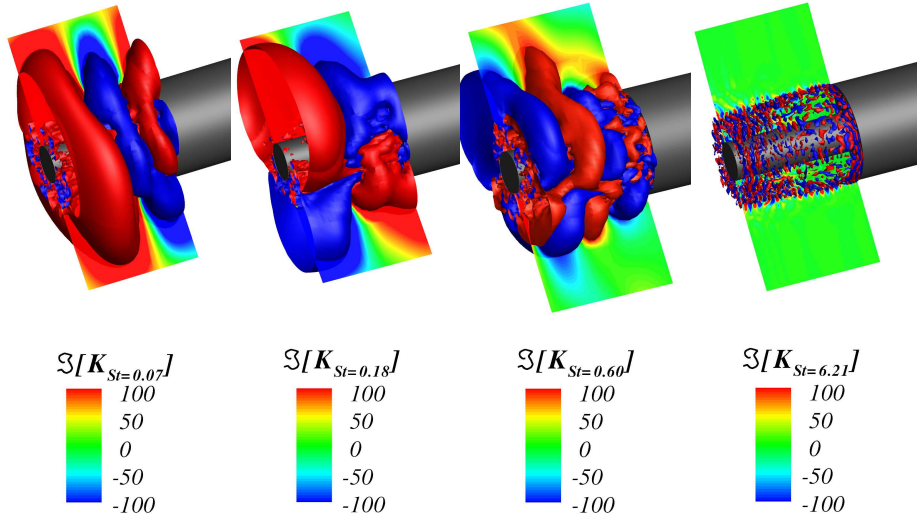


FIG. 14. DMD isosurfaces and contours of  $\Im(K_j)$  :  $St_D \simeq 0.07$ ,  $St_D \simeq 0.18$ ,  $St_D \simeq 0.60$ ,  $St_D \simeq 6.21$  (the flow goes from right to left).

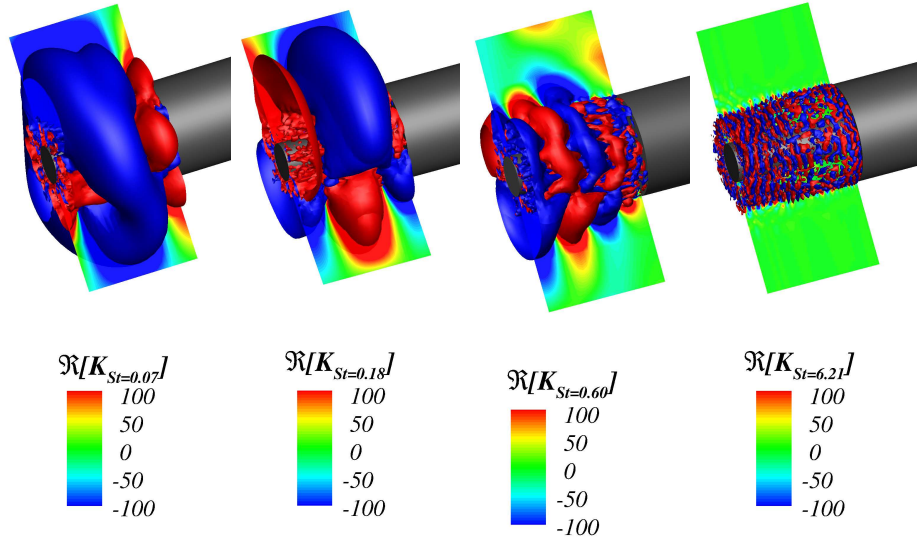


FIG. 15. DMD isosurfaces and contours of  $\Re(K_j)$  :  $St_D \simeq 0.07$ ,  $St_D \simeq 0.18$ ,  $St_D \simeq 0.60$ ,  $St_D \simeq 6.21$  (the flow goes from right to left).

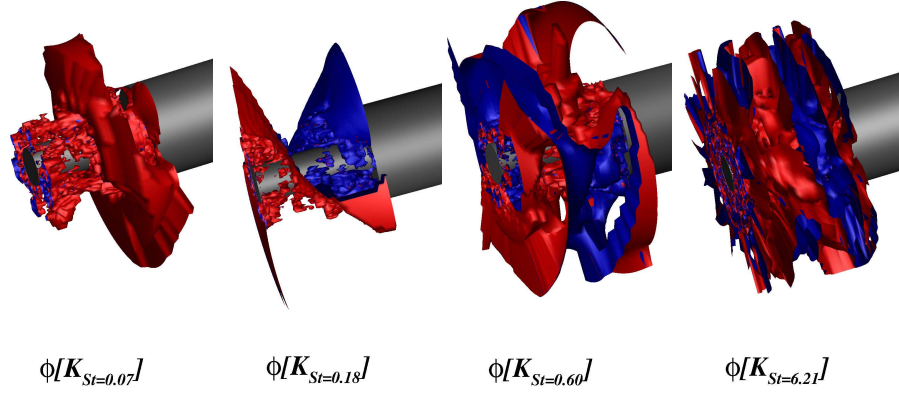


FIG. 16. DMD isosurfaces and contours of  $\phi(K_j)$  :  $St_D \simeq 0.07$ ,  $St_D \simeq 0.18$ ,  $St_D \simeq 0.60$ ,  $St_D \simeq 6.21$  (the flow goes from right to left).

## V. CONCLUSIONS

The base flow of an axisymmetric bluff body extended by a finite-length cylinder with smaller diameter has been investigated numerically using ZDES at  $Re_D = 1.2 \times 10^6$ . In particular, the detailed characteristics of the coherent structures and their intrinsic behaviour have been scrutinised.

First, the energy distribution of the fluctuating pressure at every vertex in a computational volume around the emerging cylinder was studied in both the frequency and azimuthal wave number space.

It was evidenced an energetically dominant area with  $0.4 \leq x/D \leq 0.75$  spreading in the radial direction from the wall up to the far field and associated with the vortex-shedding at  $St_D = 0.18$ . Moreover, the radial expansion of the high Power Spectral Density area with  $St_D = 0.18$  is assumed to be the consequence of the absolutely unstable nature of the vortex-shedding evidenced by Weiss *et al.*<sup>9</sup>.

Thus, the dominant azimuthal wavelength along the streamwise direction and at three radial stations is  $\lambda_\theta = \pi D/2$  which is consistent with the analysis of Deck and Thorigny<sup>8</sup> who put forward that the characteristic azimuthal wave number involves two diametrically opposed points. It was shown by means of spectra of pressure fluctuations in the azimuthal wave number space  $G_{p'}(k_\theta)$  analysis, that such an azimuthal organisation arises at several

locations around the emerging cylinder and at various range of Strouhal numbers.

In terms of azimuthal coherence, it was put forward that the most coherent dynamics is related to  $St_D = 0.18$  for the azimuthal mode  $m = 1$ . It is evidenced that the areas with the highest levels of coherence are mainly located above the mixing layer where the flow is isolated from the shear flow turbulence. It is thus inferred that the robustness of the antisymmetric dynamics in the far field deeply impacts the self-sustained pulsation of the recirculation region.

In order to elucidate the three-dimensional organisation of the fluctuating pressure field related to each of the characteristic frequencies a three-dimensional modal analysis has been performed. The reference Fourier analysis was cross-checked by a dynamic mode (DMD) analysis.

The imaginary part of the  $St_D = 0.18$  Fourier mode clearly put forward the antisymmetric distribution in the direction transverse to the flow. It occurred that the Fourier mode associated with the flapping motion of the shear layer evolves from an antisymmetric organisation close to the separation edge, to a fully axisymmetric nature on the second half of the emerging cylinder.

Thus, the assumptions made in the former studies regarding the physical interpretation of the flow dynamics using local 0D, 1D and 2D analyses have been supported using extensive spectral analyses in the three-dimensional volume surrounding the separated flow of interest.

Then, the nonlinear dynamics of a flow around an axisymmetric backward-facing step with a downstream cylinder has a large-scale helical structure as well as a hierarchy of structures at intermediate scales. This result has been illustrated by two different methods namely a decomposition into Fourier modes and a DMD study to show the robustness of the aforementioned conclusions.

Last but not least, a plot of the spectral map of the first azimuthal pressure mode  $C_{r,m=1}$  along the streamwise ( $x/D$ ) and radial ( $r/R$ ) directions for Strouhal numbers  $St_D = 0.07$  and  $St_D = 0.18$  has been performed. Such a post-processing required to compute a spectral map made with the coefficient of the two-point correlation for  $m = 1$ . This procedure allowed to determine the locations where the flapping phenomenon ( $St_D = 0.07$ ) and the shedding phenomenon ( $St_D = 0.18$ ) are dominant namely above the axisymmetric shear



layer and in the absolute instability area previously identified by Weiss *et al.*<sup>9</sup> near the middle of the emergence.

With a view to change the global dynamics of the flow, these locations constitute areas of potential receptiveness to a control device.

Finally, the helical organisation put forward by Weickgenannt and Monkewitz<sup>19</sup> in the wake of a bluff body by means of phase locked velocity was here evidenced with an alternative tool. The visualisation of the phase in the complex plane of the Fourier mode at  $St_D = 0.18$  suggested the combined translation-rotation of positive and negative fluctuating pressure patterns around the streamwise axis.

In some future work, it should be of interest to focus on the interaction between the various pressure distributions evidenced here. An analysis of the temporal reconstruction of the combined Fourier modes could lead to some insights in the modal interactions. Note that such an approach could provide improved understandings of the mechanisms responsible for the shear layer flapping motion transition from  $m = 1$  azimuthal mode to  $m = 0$ .

## ACKNOWLEDGMENTS

The authors thank the Centre National d'Etudes Spatiales (CNES) which partly funded this study within the framework of ONERA/CNES cooperation.

## Appendix A: Dynamic Modal Decomposition (DMD)

The modal decomposition of fluid dynamics is a frequently employed technique, capable of providing tools for studying dominant and coherent structures in turbulent flows. The coherent structures represent spatially or temporally evolving vortical motions, either growing with one rate, oscillating with one frequency or containing the largest possible kinetic energy. A complex turbulent flow often consists of a superposition of such coherent structures, whose development is responsible for the bulk mass, energy transfer or hydrodynamic instability. DMD is a data-driven computational technique capable of extracting dynamical information from flow fields measured in physical experiments or generated by direct numerical simulations. DMD is a powerful method of spectral decomposition, built

to represent statistically recurring and transients events. The DMD modes are extracted from the data snapshots and a unique frequency is associated to each mode.

The coherent features of turbulent separated bubble around the axisymmetric backward facing step are identified by modal decomposition techniques in order to describe the underlying mechanism. An advantage of modal decomposition is the possibility to reduce the large scale dynamics to a fewer number of degrees of freedom. To extract the coherent motion from a given dataset, we consider a sequence of  $m$  discretized and equi-distributed velocity fields  $\mathbf{u}_j = \mathbf{u}(\mathbf{x}_i, t_j) \in \mathbb{R}^n$ ,  $t_j = j\Delta t$ ,  $j = 0, 1, \dots, m-1$  as

$$\mathbf{U}_m = [\mathbf{u}_0, \mathbf{u}_1, \dots, \mathbf{u}_{m-1}] \in \mathbb{R}^{n \times m}, \quad (\text{A1})$$

where  $n$  is the total number of degrees of freedom at one time instant (number of grid points multiplied by the number of velocity components). This number is usually large compared to the number of snapshots  $m$  in the flow problem,  $n \gg m$ . In modal decomposition, the flow dynamics is splitted into space and time dependent parts as

$$\mathbf{u}(\mathbf{x}_i, t_j) = \sum_{k=0}^{m-1} \phi_k(\mathbf{x}_i) \mathbf{a}_k(t_j), \quad (\text{A2})$$

where  $\phi_k(\mathbf{x}_i)$ ,  $k = 0, \dots, m-1$  is spatial basis (the modes) and  $\mathbf{a}_k = \mathbf{a}_k(t_j)$  are temporal coefficients (amplitudes). This decomposition is not unique and depends on the choice of the base  $\phi_k$ . In DMD, the snapshots are generated by a dynamical system. It is possible, without explicit knowledge of the evolution operator, to extract frequencies, growth rates, and their related spatial structures. DMD splits the flow into different spatial modes at a given frequency. Rowley *et al.*<sup>76</sup> present the theoretical framework to compute the Koopman decomposition from a finite sequence of snapshots. Schmid<sup>77</sup> provides a more stable method to compute dynamic modes: the DMD algorithm. To compute this decomposition, a sufficiently long, but finite time serie of snapshots is considered. A time-evolving physical situation may be approximated by the action of a linear operator to the flow field  $\mathbf{u}_j$  such that

$$\mathbf{u}(\mathbf{x}_i, t_{j+1}) = \mathbf{u}_{j+1} = e^{\tilde{\mathbf{A}}\Delta t} \mathbf{u}_j = \mathbf{A} \mathbf{u}_j, \quad (\text{A3})$$

where  $\mathbf{A} = e^{\tilde{\mathbf{A}}\Delta t}$  is the evolution operator. It is then possible to write

$$\mathbf{u}(\mathbf{x}_i, t_j) = \sum_{k=0}^{m-1} \phi_k(\mathbf{x}_i) \mathbf{a}_k(t_j) = \sum_{k=0}^{m-1} \phi_k(\mathbf{x}_i) e^{i\omega_k j \Delta t} = \sum_{k=0}^{m-1} \phi_k(\mathbf{x}_i) \lambda_k^j, \quad (\text{A4})$$

where  $i\omega_k$  and  $\lambda_k$  are the eigenvalues of the matrices  $\tilde{\mathbf{A}}$  and  $\mathbf{A}$ , respectively, and the  $\phi_k$  are the corresponding eigenvectors. The relation linking the eigenvalues  $\lambda_k$  and the more familiar complex frequencies  $i\omega_k$  is

$$\lambda_k = e^{i\omega_k \Delta t}$$

It is then possible to write  $\phi_k = \mathbf{v}_k d_k$  where  $\mathbf{v}_k^T \mathbf{M} \mathbf{v}_k = 1$ . We define  $d_k$  as the amplitude and  $d_k^2$  as the energy of the dynamic mode  $\phi_k$ .

## REFERENCES

- <sup>1</sup>K. Hannemann, H. Lüdeke, J.-F. Pallegoix, A. Ollivier, H. Lambaré, J. E. J. Maseland, E. G. M. Geurts, M. Frey, S. Deck, F. F. J. Schrijer, F. Scarano, and R. Schwane, “Launch Vehicle Base Buffeting: Recent Experimental and Numerical Investigations,” Proceedings of the 7th European Symposium on Aerothermodynamics for Space Vehicles, Brugge, Belgium, 102 (2011).
- <sup>2</sup>S. Marié, P. Druault, H. Lambaré, and F. Schrijer, “Experimental analysis of the pressure-velocity correlations of external unsteady flow over rocket launchers,” Aerospace Science and Technology **30**, 83–93 (2013).
- <sup>3</sup>H. Lüdeke, J. Mulot, and K. Hannemann, “Launch Vehicle Base Flow Analysis Using Improved Delayed Detached-Eddy Simulation,” AIAA Journal **53**, 2454–2471 (2015).
- <sup>4</sup>P.-E. Weiss and S. Deck, “On the coupling of a zonal body-fitted/immersed boundary method with zdes: Application to the interactions on a realistic space launcher afterbody flow,” Comput. Fluids **176**, 338–352 (2018).
- <sup>5</sup>M. Tobak and D. Peake, “Topology of three-dimensional separated flows,” Ann. Rev. Fluid Mech. Annual Review of Fluid Mechanics, **14**, 61–85 (1982).
- <sup>6</sup>H. Choi, W.-P. Jeon, and J. Kim, “Control of flow over a bluff body,” Annual Review of Fluid Mechanics **40**, 113–139 (2008).
- <sup>7</sup>B. F. Armaly, F. Durst, J. C. F. Pereira, and B. Schönung, “Experimental and theoretical investigation of backward-facing step flow,” J. Fluid Mech. **127**, 473–496 (1983).

- <sup>8</sup>S. Deck and P. Thorigny, “Unsteadiness of an axisymmetric separating-reattaching flow,” *Phys. Fluids* **19**, 065103, doi:10.1063/1.2734996 (2007).
- <sup>9</sup>P.-É. Weiss, S. Deck, J.-C. Robinet, and P. Sagaut, “On the dynamics of axisymmetric turbulent separating/reattaching flows,” *Physics of Fluids* **21**, 075103 (2009).
- <sup>10</sup>R. D. Sandberg and H. F. Fasel, “Numerical investigation of transitional supersonic axisymmetric wakes,” *J. Fluid Mech.* **563**, 1–41 (2006).
- <sup>11</sup>D. Deprés, P. Reijasse, and J. P. Dussauge, “Analysis of unsteadiness in afterbody transonic flows,” *AIAA Journal* **42**, 2541–2550 (2004).
- <sup>12</sup>D. M. Driver, H. L. Seegmiller, and J. G. Marvin, “Time-dependent behavior of a reattaching shear layer,” *AIAA Journal* **25**, 914–919 (1987).
- <sup>13</sup>E. Achenbach, “Vortex shedding from spheres,” *J. Fluid Mech.* **62**, 209–21 (1974).
- <sup>14</sup>S. Taneda, “Visual observations of the flow past a sphere at Reynolds numbers between  $10^4$  and  $10^6$ ,” *J. Fluid Mech.* **85**, 187–192 (1978).
- <sup>15</sup>H. V. Fuchs, E. Mercker, and U. Michel, “Large-scale coherent structures in the wake of axisymmetric bodies,” *J. Fluid Mech.* **93**, 185–207 (1979).
- <sup>16</sup>P. Monkewitz, “A note on vortex shedding from axisymmetric bluff bodies,” *J. Fluid Mech.* **192**, 561–575 (1988).
- <sup>17</sup>E. Berger, D. Scholz, and M. Schumm, “Coherent vortex structures in the wake of a sphere and a circular disk at rest and under forced vibrations,” *J. Fluid Struct.* **4**, 231–257 (1990).
- <sup>18</sup>S. Cannon, F. Champagne, and A. Glezer, “Observations of large-scale structures in wake behind axisymmetrical bodies,” *Experiments in Fluids* **14**, 447–450 (1993).
- <sup>19</sup>A. Weickgenannt and P. A. Monkewitz, “Control of vortex shedding in an axisymmetric bluff body wake,” *Eur. J. Mech. B-Fluids* **19**, 789–812 (2000).
- <sup>20</sup>A. Sevilla and C. Martinez-Bazan, “Vortex shedding in high Reynolds number axisymmetric bluff-body wakes: Local linear instability and global bleed control,” *Phys. Fluids* **16**, 3460–3469 (2004).
- <sup>21</sup>A. R. Shenoy and C. Kleinstreuer, “Flow over a thin circular disk at low to moderate Reynolds numbers,” *J. Fluid Mech.* **605**, 253–262 (2008).
- <sup>22</sup>B. Pier, “Local and global instabilities in the wake of a sphere,” *J. Fluid Mech.* **603**, 39–61 (2008).
- <sup>23</sup>F. Simon, S. Deck, P. Guillen, P. Sagaut, and A. Merlen, “Numerical simulation of the

- compressible mixing layer past an axisymmetric trailing edge,” J. Fluid Mech. **591**, 215–253 (2007).
- <sup>24</sup>P. Meliga, D. Sipp, and J.-M. Chomaz, “Elephant modes and low frequency unsteadiness in a high Reynolds number, transonic afterbody wake,” Phys. Fluids **21** (2009), 10.1063/1.3139309.
- <sup>25</sup>P. Meliga, D. Sipp, and J. M. Chomaz, “Effect of compressibility on the global stability of axisymmetric wake flows,” J. Fluid Mech. **660**, 499–526 (2010).
- <sup>26</sup>R. Pain, P.-E. Weiss, and S. Deck, “Three-dimensional spectral analysis of an axisymmetric separating/reattaching flow,” TSFP 8, International Symposium On Turbulence and Shear Flow Phenomena (2013).
- <sup>27</sup>R. Pain, P.-E. Weiss, and S. Deck, “Zonal Detached Eddy Simulation of the flow around a simplified launcher afterbody,” AIAA Journal **52**, 1967–1979 (2014).
- <sup>28</sup>V. Statnikov, T. Sayadi, M. Meinke, P. Schmid, and W. Schröder, “Analysis of pressure perturbation sources on a generic space launcher after-body in supersonic flow using zonal turbulence modeling and dynamic mode decomposition,” Physics of Fluids **27**, 016103 (2015).
- <sup>29</sup>G. Yun, D. Kim, and H. Choi, “Vortical structures behind a sphere at subcritical Reynolds numbers,” Physics of Fluids **18**, 015102 (2006).
- <sup>30</sup>V. Statnikov, M. Meinke, and W. Schröder, “Reduced-order analysis of buffet flow of space launchers,” Journal of Fluid Mechanics **815**, 1–25 (2017).
- <sup>31</sup>J. Seidel, S. Siegel, T. Jeans, S. Aradag, K. Cohen, and T. McLaughlin, “Analysis of an Axisymmetric Bluff Body Wake using Fourier Transform and POD,” 46th AIAA Aerospace Sciences Meeting and Exhibit, AIAA Paper , 2008–552 (2008).
- <sup>32</sup>S. C. Cannon, *Large-Scale Structures and the Spatial Evolution of Wakes behind Axisymmetric Bluff Bodies*, Ph.D. thesis, University of Arizona (1991).
- <sup>33</sup>V. Gentile, F. F. J. Schrijer, B. W. van Oudheusden, and F. Scarano, “Afterbody effects on axisymmetric base flows,” AIAA Journal **54**, 2285–2294 (2016).
- <sup>34</sup>M. Grandemange, M. Gohlke, and O. Cadot, “Statistical axisymmetry of the turbulent sphere wake,” Experiments in Fluids **55** (2014), 10.1007/s00348-014-1838-x.
- <sup>35</sup>M. Grandemange, M. Gohlke, V. Parezanović, and O. Cadot, “On experimental sensitivity analysis of the turbulent wake from an axisymmetric blunt trailing edge,” Physics of Fluids **24**, 035106 (2012).

- <sup>36</sup>M. Grandemange, M. Gohlke, and O. Cadot, “Turbulent wake past a three-dimensional blunt body. part 1. global modes and bi-stability,” *Journal of Fluid Mechanics* **722**, 51–84 (2013).
- <sup>37</sup>V. Gentile, F. F. J. Schrijer, B. W. V. Oudheusden, and F. Scarano, “Low-frequency behavior of the turbulent axisymmetric near-wake,” *Physics of Fluids* **28**, 065102 (2016).
- <sup>38</sup>V. Gentile, B. W. van Oudheusden, F. F. J. Schrijer, and F. Scarano, “The effect of angular misalignment on low-frequency axisymmetric wake instability,” *Journal of Fluid Mechanics* **813** (2017), 10.1017/jfm.2017.4.
- <sup>39</sup>G. Rigas, A. R. Oxlade, A. S. Morgans, and J. F. Morrison, “Low-dimensional dynamics of a turbulent axisymmetric wake,” *Journal of Fluid Mechanics* **755** (2014), 10.1017/jfm.2014.449.
- <sup>40</sup>G. Rigas, A. S. Morgans, R. D. Brackston, and J. F. Morrison, “Diffusive dynamics and stochastic models of turbulent axisymmetric wakes,” *Journal of Fluid Mechanics* **778** (2015), 10.1017/jfm.2015.390.
- <sup>41</sup>G. Rigas, A. S. Morgans, and J. F. Morrison, “Weakly nonlinear modelling of a forced turbulent axisymmetric wake,” *Journal of Fluid Mechanics* **814**, 570–591 (2017).
- <sup>42</sup>P. E. Weiss and S. Deck, “Numerical investigation of the robustness of an axisymmetric separating/reattaching flow to an external perturbation using ZDES,” *Flow, Turbulence and Combustion* **91**, 697–715 (2013).
- <sup>43</sup>S. Deck, “Zonal-Detached-Eddy Simulation of the flow around a high-lift configuration,” *AIAA Journal* **43**, 2372–2384 (2005).
- <sup>44</sup>S. Deck, “Recent improvements in the Zonal Detached Eddy Simulation (ZDES) formulation,” *Theor. Comp. Fluid Dyn.* **26**, 523–550 (2012).
- <sup>45</sup>V. Statnikov, I. Bolgar, S. Scharnowski, M. Meinke, and W. Kähler C. J. Schröder, “Analysis of characteristic wake flow modes on a generic transonic backward-facing step configuration,” *Eur. J. Mech. B/Fluids* **55**, 124–134 (2016).
- <sup>46</sup>P. Meliga and P. Reijasse, “Unsteady transonic flow behind an axisymmetric afterbody with two boosters,” (2007).
- <sup>47</sup>S. K. Lele, “Compact finite differences schemes with spectral-like resolution,” *Journal of Computational Physics* **103**, 16–42 (1992).
- <sup>48</sup>S. C. Morris and J. F. Foss, “Turbulent boundary layer to single-stream shear layer: The transition region,” *Journal of Fluid Mechanics* **494** (2003).

- <sup>49</sup>P. Holmes, J. L. Lumley, and G. Berkooz, “Coherent Structures, Symmetry: Dynamical Systems and Turbulence,” Cambridge University Press, Cambridge (1992).
- <sup>50</sup>S. Scharnowski, V. Statnikov, M. Meinke, W. Schröder, and C. J. Kähler, “Combined experimental and numerical investigation of a transonic space launcher wake,” *Progress in Flight Physics* **7**, 1–18 (2015).
- <sup>51</sup>P. Guillen and M. Dormieux, “Design of a 3d multi-domain euler code,” in *International Seminar of Supercomputing, Boston, USA* (1989).
- <sup>52</sup>M.-S. Liou, “A sequel to AUSM: AUSM+,” *J. Comp. Phys.* **129**, 364–382 (1996).
- <sup>53</sup>P. Weiss and S. Deck, “Control of the antisymmetric mode ( $m=1$ ) for high reynolds axisymmetric turbulent separating/reattaching flows,” *Phys. Fluids* **23**, 095102 (2011).
- <sup>54</sup>P. Sagaut, S. Deck, and M. Terracol, *Multiscale and multiresolution approaches in turbulence: Applications and Guidelines (2nd Edition)* (Imperial College Press, 2013).
- <sup>55</sup>S. Deck, F. Gand, V. Brunet, and S. B. Khelil, “High-fidelity Simulations of Unsteady Civil Aircraft Aerodynamics: Stakes and Perspectives. Application of Zonal Detached Eddy Simulation (ZDES),” *Philosophical Transactions of the Royal Society A* **372**, 2022 (2014).
- <sup>56</sup>S. Deck, N. Renard, R. Laraufie, and P.-E. Weiss, “Large-scale contribution to mean wall shear stress in high-Reynolds-number flat-plate boundary layers up to  $Re_\theta = 13650$ ,” *Journal of Fluid Mechanics* **743**, 202–248 (2014).
- <sup>57</sup>S. Deck, N. Renard, R. Laraufie, and P. Sagaut, “Zonal detached eddy simulation (ZDES) of a spatially developing flat plate turbulent boundary layer over the Reynolds number range  $3150 \leq Re_\theta \leq 14000$ ,” *Phys. Fluids* **26**, 025116 (2014).
- <sup>58</sup>S. Deck and R. Laraufie, “Numerical investigation of the flow dynamics past a three-element airfoil,” *J. Fluid Mech.* **732**, 401–404 (2013).
- <sup>59</sup>L. M. Hudy, A. M. Naguib, and W. M. Humphreys, “Wall-pressure-array measurements beneath a separating/reattaching flow region,” *Physics of Fluids* **15**, 706–717 (2003).
- <sup>60</sup>D. Mabey, “Analysis and correlation of data on pressure uctuations in separated ow,” *J. Aircr.* **9**, 642 (1972).
- <sup>61</sup>R. Coe, “The effects of some variations in launch-vehicle nose shape on steady and uctuating pressures,” NASA Technical Memorandum **TMX-636** (1962).
- <sup>62</sup>S. Marié, S. Deck, and P.-E. Weiss, “From pressure fluctuations to dynamic loads on axisymmetric step flows with minimal number of kulites,” *Comput. Fluids* **39**, 747–755

(2010).

- <sup>63</sup>P. Huerre and M. Rossi, *Hydrodynamics and Nonlinear Instabilities* (Cambridge University Press, 1998) pp. 81–294.
- <sup>64</sup>P. Sagaut and S. Deck, “Large Eddy Simulation for aerodynamics: status and perspectives,” *Phil. Trans. R. Soc. A* **367**, 2849–2860. doi:10.1098/rsta.2008.0269 (2009).
- <sup>65</sup>P. Huerre and P. A. Monkewitz, “Absolute and convective instabilities in free shear layers,” *J. Fluid Mech.* **159**, 151–168 (1985).
- <sup>66</sup>L. Larchevêque, P. Sagaut, T. H. Le, and P. Comte, “Large-eddy simulation of a compressible flow in a three-dimensional open cavity at high reynolds number,” *J. Fluid Mech.* **516**, 265–301 (2004).
- <sup>67</sup>L. H. Koopmans, “The spectral analysis of time series,” (Academic Press, 1995).
- <sup>68</sup>P. D. Welch, “The use of Fast Fourier Transform for the estimation of power spectra: A method based on time averaging over short, modified periodograms,” *IEEE Transactions on Audio and Electroacoustics* **AU-15**, 70–73 (1967).
- <sup>69</sup>S. G. Johnson, “Notes on FFT-based differentiation,” Department of Mathematics, MIT (2011).
- <sup>70</sup>D. Marshall and T. E. Stanton, “On the Eddy System in the Wake of Flat Circular Plates in Three Dimensional Flow,” *Proc. R. Soc. Lond. A* **130**, 295–301 (1931).
- <sup>71</sup>L. Rosenhead, “Vortex Systems in Wakes,” *Advances in Applied Mechanics* **3**, 185–195 (1953).
- <sup>72</sup>H. Sakamoto and H. Haniu, “A Study on Vortex Shedding From Spheres in a Uniform Flow,” *Journal of Fluids Engineering* **112**, 386–392 (1990).
- <sup>73</sup>C. Mettot, D. Sipp, and H. Bizard, “Quasi-laminar stability and sensitivity analyses for turbulent flows: Prediction of low-frequency unsteadiness and passive control.” *Physics of Fluids* **26**, 045112 (2014).
- <sup>74</sup>S. Beneddine, D. Sipp, A. Arnault, J. Dandois, and L. Lesshafft, “Conditions for validity of mean flow stability analysis.” *J. Fluid Mech.* **798**, 485–504 (2016).
- <sup>75</sup>B. McKeon, “The engine behind (wall) turbulence: Perspectives on scale interactions.” *J. Fluid Mech.* **817**, P2 (2017).
- <sup>76</sup>C. W. Rowley, I. Mezić, S. Bagheri, P. Schlatter, and D. S. Henningson, “Spectral analysis of nonlinear flows,” *J. Fluid Mech.* **641**, 115–127 (2009).
- <sup>77</sup>P. J. Schmid, “Dynamic mode decomposition of numerical and experimental data,” *J. Fluid*



- Mech. **656**, 5–28 (2010).
- <sup>78</sup>K. K. Chen, J. H. Tu, and C. W. Rowley, “Variants of Dynamic Mode Decomposition: Boundary condition, Koopman, and Fourier analyses,” J. Nonlinear Sci. **22**, 887–915 (2012).
- <sup>79</sup>K. K. Chen, J. H. Tu, and C. W. Rowley, “Variants of dynamic mode decomposition: boundary condition, koopman, and fourier analyses,” Journal of Nonlinear Science **22**, 887–915 (2012).
- <sup>80</sup>G. Aubard, J. C. Robinet, and X. Gloerfelt, “Physical insight into the unsteady shock-wave turbulent boundary layer interaction using Large Eddy Simulation,” in *Proceedings of the 7th International Symposium on Turbulence and Shear Flow Phenomena, Ottawa, Canada* (2011).
- <sup>81</sup>P. J. Schmid, L. Li, M. P. Juniper, and O. Pust, “Applications of the dynamic mode decomposition,” Theor. Comput. Fluid Dyn. **25**, 249–259. doi:10.1007/S00162-010-0203-9 (2011).